Summer 8-2-2012

Theoretical Approaches to the Characterization of Water, Aqueous Interfaces, and Improved Sampling of Protein Conformational Changes

Alexis J. Lee
UNIVERSITY OF NEW ORLEANS, AJLEE1@UNO.EDU

Theoretical Approaches to the Characterization of Water, Aqueous Interfaces, and Improved Sampling of Protein Conformational Changes

A Dissertation

Submitted to the Graduate Faculty of the
University of New Orleans
in partial fulfillment of the
requirments for the degree of

Doctor of Philosophy
in
Chemistry

by

Alexis J. Lee

B.S. University of Louisiana, Lafayette, 2006

August, 2012

For Seymour and his Fat Lady...

Acknowledgments

When I consider all the people to whom I owe thanks for getting me to this point in my life and education, quite a lengthy list compounds. First and foremost, I offer my sincerest gratitude to my advisor, Professor Steve W. Rick, who has guided me in so many ways throughout my graduate career. Imparting his knowledge, wisdom, and time are things for which I am eternally grateful. I could not have asked for a more understanding and patient advisor. I very much appreciate my committee, Professor David Mobley, Professor Chris Summa, and Professor Edwin Stevens, for their time and input. Thanks are owed to the University of New Orleans Department of Chemistry for five wonderful years.

My dear friend and former lab mate, Dr. Hongtao Yu, deserves special acknowledgement. He helped me so much in learning Fortran, in classes, and taught me about Chinese culture. My current lab mates, Marielle Soniat, Kalika Murthy Aritakula, Dr. Sreeja Parameswaran, I just adore. Thank you for being so friendly and making my last few years so joyous.

Expressing my gratitude to my parents is of utmost importance. They have been the most amazing support system and role models. Both such hard-working and beautiful people–something for which I strive. My mother and father have loved me unconditionally, with patience, tolerance, and understanding and were there for me when I needed them, without question. My brother, his wife, and their precious baby have been a source of inspiration for the last few years. Lastly, I would like to acknowledge my undergraduate advisor, Professor Richard S. Perkins, for showing me scientists are, above all, interesting people.

Table of Contents

List of Figures

List of Tables

Abstract

Methods to advance the understanding of water and other aqueous systems are developed. This work falls into three areas: The creation of better interaction potentials for water, the development of superior methods for sampling configurational space, and the applications of these methods to understand systems of interest. Charge transfer has been shown by *ab initio* methods to be important in the water–water and water–ion interactions. A model for treating charge transfer in liquid water and aqueous systems is presented in this manuscript. The model is called Discrete Charge Transfer (DCT) and is based on the commonly-used TIP4P/2005 model, which represents the charge distribution of water molecules with three charge sites. Such models have been very successful in reproducing many of the physical properties of water. Charge transfer is introduced by transferring a small amount of charge, -0.02 e, from the hydrogen bond acceptor to the hydrogen bond donor, as has been indicated by electronic structure calculations. We have parameterized both polarizable and non-polarizable potentials, optimized to include charge transfer. Methods to surmount the obstacles incurred by the introduction of charge transfer, which involve the amount of charge transfer at large distances and implementation into Molecular Dynamics simulation, is presented, along with our results assessing the importance of charge transfer in liquid water and aqueous systems. Also presented is a method for improving efficiency of a sampling technique, Replica Exchange, by reducing the number of replicas. The improved method is called Replica Exchange with Driven Scaling (REDS2).

Keywords: Molecular Dynamics, Charge Transfer, Water, REDS2

Chapter 1

Introduction

Molecular simulation is a powerful tool. The evolution of technologies has led to an ever-increasing demand for more efficient methods of understanding the microscopic realm. "Experiments do not always come with explanations," an apothegm of science, is itself an adequate impetus to search for more innovative means by which data may be obtained. Microscopic length- and timescales are now accessible for exploration, due to increased sophistication of computers, bridging the microscopic world and the macroscopic realm of the laboratory. Detailed characterization of structural information and interactions on the microscopic scale can be costly, difficult, or impossible to obtain by conventional methods. Simulated experimentation techniques are aimed at gaining understanding of the properties of molecular systems by methods that can complement or even replace laboratory approaches.

Two classes of computational methods for obtaining valuable molecular information, the latter of which is of principal concern, are *ab initio* (quantum principles) calculations and empirical potential energy models. First principles techniques are purely theoretical, in that no experimental data is involved in the computation of system properties. *Ab initio* calculations alone, though extremely robust, are computationally expensive and cannot provide dynamical information about a system. Fortunately, a cheaper approach exists. Empirical potential models employ both experimental and theoretical data. Potentials, or force fields,

are a set of mathematical functions and parameters designed to describe the potential energy of a system of particles.[13, 14, 15, 16, 17, 18]

Molecular simulations are limited by the accuracy of the potential energy model which is used. The development of accurate yet computationally efficient models is a constant challenge. Results of molecular simulation can be sensitive to such factors as the model utilized, how a surface is defined, the definition of a hydrogen bond, and polarizability, leading to qualitatively different results, especially for anions at liquid water/air interfaces.[19, 20, 21, 22, 23] Molecular simulations can also be affected by the timescale of the model. Two ways to surmount this issue are to build more efficient potentials or use faster, more efficient sampling techniques. My research over the last 5 years has focused on the development of the following:

- DCT (Discrete hydrogen-bond-based Charge Transfer): A new water potential that treats charge transfer (CT) in hydrogen-bonded and asymmetrically-bonded systems.[24]
- REDS2 (Replica Exchange with Dynamical Scaling): A simulation technique which improves the efficiency of conventional replica exchange (RE) by reducing the number of replicas.[25]

The new model, Discrete Charge Transfer[24], or DCT, was parameterized for the non-polarizable and polarizable potentials, TIP4P[6] and TIP4P-FQ[7], respectively, and applied to the study of aqueous bulk and interfacial charge transfer.

Aqueous interfaces are often the home of curious chemical processes in nature[26], including electrochemical reactions associated with aqueous batteries[27], protein solvation and folding[28, 29] and "on water" organic catalysis.[30, 31, 32] Despite extensive experimental and theoretical research on interfaces, an accurate depiction of the air/water interface has yet to be agreed upon by the scientific community. The need for a proper understanding of the structure and chemistry of the air/water interface is relevant to many fields of study, such as atmospheric chemistry, biochemical processes, and electrokinetics.[33]

Since the 19th century, scientists have observed a counterintuitive electrokinetic phenomenon that occurs when air bubbles and oil droplets in water are subjected to an external electric field. The air bubbles and oil droplets exhibit negative electrophoretic mobility, acting as negatively-charged colloidal particles.[34, 35, 36, 37] Numerous explanations have been proposed as to why the bubbles and droplets drift toward the cathode. Theories put forth include aggregation of OH^- at the surface, the existence of a diffuse (or shear) layer of OH^- just below the surface[38, 39, 40, 41], and dipole ordering of the surface water molecules[42], none of which offers a satisfactory explanation of all the physical properties observed at the interface. Spectroscopic data suggest that the first two or three molecular layers near the interface are populated by hydronium ions, while approximately 10-20 Å into the bulk, hydroxide ions counterbalance a more positive surface under normal pH conditions. Hydroxide at the surface would produce opposite behavior.[43, 44, 45, 46, 47, 48, 49, 50, 51, 52]

Recent *ab initio* molecular dynamics (AIMD) simulations have reported dangling O–H bonds (non-hydrogen-bonded surface [water] hydrogens) at the liquid/vapor interface, consistent with surface-specific vibrational sum-frequency generation (SFG) data.[33] Such asymmetrically-bonded surface water molecules will be discussed later in this text. As mentioned previously, spectroscopic and theoretical experiments of small clusters and larger water systems predict higher concentration of hydronium ions at the surface.[43, 44, 45] Such predictions, however, do not explain the electrophoretic mobility of air bubbles toward the cathode. Understanding the electrokinetic properties of water is the crux of the fundamental debate over whether the surface of water is acidic or basic.

A 2009 submission to *Chemical Physics Letters* (*CPL*) by Richard Saykally[53] acknowledged the intense controversy over the surface structure of water, and consequently, had an entire issue of *CPL* dedicated to this dispute. The July 2010 issue of *C&EN Magazine* featured the tumultuous debate in an article aptly titled, "Storm in a Teacup," where scientists from both camps–Waters surface: Acidic or Basic?–presented justifications for their theories regarding the surface structure of water.[54] We have joined this discussion by sug-

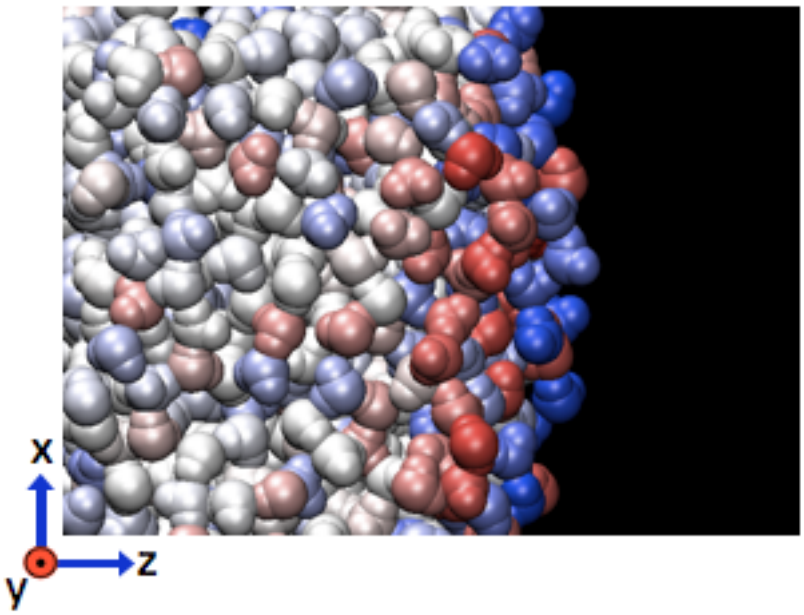

Figure 1.1: Aggregation of partial positive charge (blue) at the air/water interface with a negatively-charged (red) layer beneath the surface; charges disperse into the bulk, averaging to neutrality.

gesting that charge transfer (CT) between neighboring water molecules at the air/water interface may have an effect on the total interfacial charge, giving rise to a response to an external/applied electric field [55], as in Figure 1.1.

We assert that including charge transfer in a water potential, particularly a polarizable model, leads to the observation of important physical effects not captured by previous potentials for water that do not consider charge transfer. Implementation of our newly-developed potentials, TIP4P+DCT (discrete hydrogen-bond-based charge transfer with TIP4P[6] water) and TIP4P-FQ[7]+DCT (fluctuating charge TIP4P water plus DCT), in the characterization of aqueous interfaces (liquid/vapor, ice/vapor, ice/liquid) is presented in this dissertation. A method for improving a protein conformation sampling technique, replica exchange (RE), using our driven scaling method, REDS2, is also discussed.[25] Through in-depth analyses of the water and aqueous systems mentioned, we have gained better insight into the surface chemistry and structure of water and the energetic, structural, chemical, and physical consequences of charge transfer.

Chapter 2

Background and Theory

2.1 Potential Energy Models and Force Fields

2.1.1 Describing a System Mathematically

In principle, the entirety of information of an isolated system can be obtained by solving the system's time-dependent Schrödinger equation[56],

$$\hat{\mathcal{H}}\Psi = i\hbar\frac{\partial\Psi}{\partial t}\,, \tag{2.1}$$

where $\hat{\mathcal{H}}$ is the Hamiltonian operator, which operates on the wavefunction, Ψ, for the system, i is the imaginary number equal to $\sqrt{-1}$, $\hbar$ is the Dirac constant equivalent to h (Planck's constant) divided by 2π, and t is time. In classical Hamiltonian mechanics, a wavefunction (Ψ) is a mathematical function that describes the state of a particle at time t, given by the following vectors: $\mathbf{r}(x, y, z)$, the position, and $\mathbf{p}(p_x, p_y, p_z)$, the momentum.[57]

The dynamics of all particles of a system, both slow-moving nuclei (heavy) and fast-moving electrons (light), abide by Schrödinger's equation. Solving the time-dependent Schrödinger equation (Equation 2.1) for the wavefunction can be a difficult task, as systems become increasingly more complex–meaning anything larger than a single electron in one dimension. Fortunately, the Born–Oppenheimer approximation[58] provides a shortcut to solving quantum mechanical calculations. With the Born–Oppenheimer approximation,

the wavefunction may be obtained easier because the dynamics of the nuclei and electrons are addressed separately, disconnecting the differing timescales caused by an immense mass difference. The total wavefunction, Ψ_{tot}, then becomes the sum of its parts,

$$\Psi_{tot}(nuclei, electrons) = \Psi(nuclei)\Psi(electrons)\ . \tag{2.2}$$

The electronic equation may be written as

$$\hat{\mathcal{H}}_{el}\Psi_{el} = E_{el}(\mathbf{r}_1, \mathbf{r}_2, \ldots \mathbf{r}_N)\Psi_{el}\ , \tag{2.3}$$

providing the electronic Hamiltonian, $\hat{\mathcal{H}}_{el}$, electronic wavefunction, Ψ_{el}, and electronic energy, E_{el}.[18] A similar equation may be written for the nucleic motion.

2.1.2 Exploring the Potential Energy Surface

Severance of the nuclear and electronic pieces of the overall wavefunction allows for exploration of the potential energy surface, which is essentially an effective potential felt by the nuclei without the effects of individual electrons.[14, 15, 18, 57]

$$\hat{\mathcal{H}}(\mathbf{p}_i, \mathbf{r}_i) = \sum_{i=1}^{N} \frac{1}{2m_i}\mathbf{p}_i^2 + \mathcal{V}(\mathbf{r}_i) \tag{2.4}$$

The Hamiltonian operator ($\hat{\mathcal{H}}$) in Equation 2.4 is defined as a function of $\mathbf{p}_i$ and $\mathbf{r}_i$, the momentum and position of particle i, respectively, and $\mathcal{V}(\mathbf{r}_i)$ is the potential obtained from *ab initio* calculations or by empirical means, discussed later in this chapter. For a system of N particles, with i varying from 1 to N, 6N independent variables are requisite for defining that system – 3N particle coordinates and 3N momenta constituents.

The combination of the 6 variables comprising $\Psi(\mathbf{p}, \mathbf{r})$ yields the description of exactly one point at time t in a six-dimensional space. The way in which the system moves through phase space is governed by Hamilton's equations. Hamilton's first-order differential equations

are

$$\dot{\mathbf{p}}_i = -\frac{\partial \mathcal{H}}{\partial \mathbf{r}_i} = -\frac{\partial \mathcal{V}}{\partial \mathbf{r}_i} = \mathbf{f}_i \tag{2.5}$$

and

$$\dot{\mathbf{r}}_i = -\frac{\partial \mathcal{H}}{\partial \mathbf{p}_i} = \frac{\dot{\mathbf{p}}_i}{m_i} \,. \tag{2.6}$$

By taking the time derivative of Equation 2.6, followed by substitution of the momentum of the system $\dot{\mathbf{p}}_i$ into Equation 2.5, we arrive at Newton's Second Equation of Motion,

$$\mathbf{f}_i = m_i \ddot{\mathbf{r}}_i \,, \tag{2.7}$$

a fundamental classical-mechanical equation.[13, 17, 18]

Although they constitute an approximation to the real dynamics, classical dynamical simulation techniques are believed to provide accurate descriptions in many cases.[18]

2.2 Obtaining Molecular Data

2.2.1 *Ab Initio* Calculations

Information about a system may be derived by purely theoretical methods called *ab initio* quantum chemistry. Such methods stem from first principles of quantum mechanics and use no experimental data to solve the Schrödinger equation exactly. A goal of *ab initio* techniques is to employ the fewest number of approximations as possible. First principles approaches are useful because convergence to the exact solution can be achieved using proper basis sets and level of theory. Though these electronic structure calculations are very powerful, dynamical information cannot be obtained by *ab initio* calculations alone.

2.2.2 Potential Energy Models

Quantum-mechanical methods are very effective for relatively small systems (up to approximately 100 molecules). A wealth of information may be gained because all particles,

neutrons and electrons, are considered. However, as system size increases, *ab initio* approaches become too computationally expensive. A cheaper alternative approach applicable to large molecular systems is the employment of potential energy models (also called force fields in molecular mechanics simulation). A combination of empirical and *ab initio* data is used to build a force field. The parameterized potential model is constructed to mimic reality as closely as possible. The potential energy function, $\mathcal{V}(\mathbf{r}_i)$, of an empirical force field employs experimental and theoretical data, unlike quantum methods.

If the positions, $\mathbf{r}$, and momenta, $\mathbf{p}$, of the nuclear variables are known, the Hamiltonian may be expressed as

$$\mathcal{H}(\mathbf{p},\mathbf{r}) = \mathcal{K}(\mathbf{p}) + \mathcal{V}(\mathbf{r})\,, \tag{2.8}$$

and equations of motion can be derived using the kinetic and potential energy components, $\mathcal{K}(\mathbf{p})$ and $\mathcal{V}(\mathbf{r})$, respectively. Utilizing Equation 2.8, the microscopic system can be tracked over time, and the mechanical properties can be determined. Consider a system of N particles, consisting of particles i, j, k, etc.. The potential energy for that system may be given by

$$\mathcal{V} = \sum_i v_1(\mathbf{r}_i) + \sum_i \sum_{j>i} v_2(\mathbf{r}_i,\mathbf{r}_j) + \sum_i \sum_{j>i} \sum_{k>j>i} v_3(\mathbf{r}_i,\mathbf{r}_j,\mathbf{r}_k) + \ldots \tag{2.9}$$

Each particle pair is handled individually and will not be repeated when counting interactions for the system. In Equation 2.9, $\sum_i v_1(\mathbf{r}_i)$ denotes the effects of any external field the system may experience. The second term containing v_2 is the pair potential, which is dependent upon $r_{ij} = |\mathbf{r}_i - \mathbf{r}_j|$, the magnitude of the pair separation. Liquids depend on the third non-additive potential term containing v_3, the triplet term. Four-body interaction terms and higher tend to be smaller than v_2 and v_3. Summing over triplets can be computationally expensive, so the higher many-body calculations may be excluded.[13]

Bonded Interactions

Intermolecular interactions are represented in empirical force fields as bonding and non-bonding in terms of pairs, triplets, and so on. Each bonded pair has its own potential energy components. Because chemical bonds may be free to rotate or bend, the energy for this must be counted. Total covalent bond energy terms include energy of the covalent bond, bond angle, dihedral angle, and distortion. The summation of the energy terms follows the form

$$\mathcal{V}_{cov} = \mathcal{V}_{bond} + \mathcal{V}_{angle} + \mathcal{V}_{dihedral} + \mathcal{V}_{impropers} \, . \tag{2.10}$$

Bonded pairs of atoms can be treated as springs with force constants, like harmonic oscillators. Some potentials use rigid-body molecules, meaning all bond lengths and angles are fixed. Use of rigid-body molecules eliminates the angle and bond terms in Equation 2.10. However, if the molecule is allowed to bend, an angle term for the energy would be

$$\mathcal{V}_{angle} = \sum_{angles} \frac{1}{2} k_\theta (\theta - \theta_0)^2 \, , \tag{2.11}$$

where k_0 is the force constant for the angle, and θ_0 is the equilibrium bond angle. Note the summation is over all angles. For simulation of larger molecules or proteins, a dihedral potential energy term may be necessary. Some molecular mechanics force fields do not include torsional terms to the potential.[16]

$$\mathcal{V}_{dihedrals} = \sum_{dihedral} \frac{1}{2} V_n [1 + cos(n\phi - \delta)] \tag{2.12}$$

In Equation 2.12, V_n is the force constant, n is the periodicity of the angle (ϕ), and δ is the phase of the angle. The periodicity determines the number of peaks in the potential.[18, 59] For some planar groups of atoms, planarity is maintained with an improper dihedral angle term,

$$\mathcal{V}_{impropers} = \sum_{impropers} \frac{1}{2} V_n [1 + cos(n\omega - \delta)] \, , \tag{2.13}$$

in which the distorted dihedral angle is ω.

Non-bonded Interactions

Particle-particle interactions that take place between non-bonded molecules are said to be non-bonding interactions. The non-bonding interactions are most important in affecting the characteristic behavior of a system. Potentials generally include

$$\mathcal{V}_{total} = \sum_{i \neq j}^{N} (\mathcal{V}_{elec} + \mathcal{V}_{LJ} + \mathcal{V}_{pol}) \tag{2.14}$$

an electrostatic part (charge-charge), the Lennard-Jones potential (long-range attractive, short-range repulsive interactions), and a polarization part (dipole-dipole). Long-range forces usually have an interaction that falls off with r^{-d}, where d is the length of the simulation cell. Charge-charge interactions approximately fall off as r^{-1} and dipole-dipole at a rate of r^{-3}.[13, 16] The charge-charge, or Coulombic, part of the potential is commonly written as

$$\mathcal{V}_{elec} = \frac{1}{4\pi\epsilon_0} \frac{q_i q_j}{r} \,, \tag{2.15}$$

where q_i and q_j are the charges of particles i and j, r is the radius between i and j, and ϵ_0 is the permittivity of free space. The Lennard-Jones potential as a function of the particle-particle radius, r, is

$$\mathcal{V}_{LJ}(r) = 4\epsilon \left[\left(\frac{\sigma}{r}\right)^{12} - \left(\frac{\sigma}{r}\right)^{6} \right] \,, \tag{2.16}$$

where σ is the separation at which the Lennard-Jones potential changes sign. The variable, ϵ, is depth of the potential well. Polarization and charge transfer are two other non-bonded interactions, which will be described in more detail later.

2.3 Molecular Dynamics Simulations

In order to obtain equilibrium transport and thermodynamic properties of a system, a useful simulation technique is Molecular Dynamics (MD).[17] Molecular Dynamics generates

a sequence of configurations of a system by integrating Newton's Laws of Motion. A potential describes each particle of the system as a point with mass, spatial coordinates, and equations of motion. Newton's Second Law,

$$\frac{d^2x_i}{dt^2} = \frac{F_{x_i}}{m_i}\,, \tag{2.17}$$

is integrated at each timestep to generate a new trajectory for each particle of mass m_i. The force, F_{x_i}, acts on a particle along the coordinate, x_i, at a time, t.

2.4 Water Potentials

A relatively elementary water model called simple point charge (SPC) was developed by Berendsen *et al.*[60] in 1981. SPC is a rigid, 3-site (3 interaction sites) potential, where each site has a fixed charge. The three atoms of the water molecule are charge sites with one Lennard-Jones center at the oxygen position. The geometry of SPC is that of the ideal tetrahedral shape, with an H–O–H bond angle of 109.47°.

Published in 1983 by Jorgensen, *et al.* were the TIPS force fields – TIPS2, TIP3P, and TIP4P.[6] TIP3P (3-point-transferable-intermolecular-potential) is a rigid 3-site model with an optimized geometry closer to the experimental H–O–H angle, 104.5°, rather than the ideal tetrahedral geometry, with fixed charges on atom sites. TIP4P (4-point-transferable-intermolecular-potential) is a rigid 4-site model with three charge sites and a Lennard-Jones center. The oxygen charge, however, is placed on an M-site slightly off the oxygen in a position bifurcating the H–O–H angle, making the oxygen site only the Lennard-Jones center.

Researchers came to realize the inclusion of polarization effects led to more accurate data. SPC was improved upon by adding a polarization correction factor (Equation 2.18) to the potential energy function and dubbed SPC/E.[61]

$$\mathcal{V}_{pol} = \sum_{i=1}^{N} \frac{(\mu_i - \mu_{gp})^2}{2\alpha} \tag{2.18}$$

The dipole moment of the model and dipole moment of the gas phase are denoted μ_i and μ_{gp}, respectively, and α is the polarizability. Charges for the models, SPC, SPC/E, TIP4P, *et cetera*, are parameterized to fit data and do not correspond to the gas phase values, reflecting, perhaps, the enhanced charges due to polarization. Adding the polarization term allows for proper accounting of the energy required to polarize the charges and tends to improve the model. Recent successful models use this correction, e.g., TIP4P/2005[2] and TIP4P-Ew[3].

A fluctuating-charge potential, fluc-q, was parameterized for both SPC and TIP4P by Rick, Stuart, and Berne in 1994[7]. Polarizability is included in the model by allowing the charges to fluctuate, or respond to the changing electrostatic field that arises from movement of the particles in a system.

Chapter 3

The Effects of Charge Transfer on the Properties of Liquid Water

3.1 Introduction

The factors which determine interaction strengths among molecules and the development of accurate potential models are important in understanding and predicting the properties of the condensed phases. For small systems, like the water dimer, *ab initio* methods can be used to analyze the intermolecular interactions.[62, 63, 64, 65, 66, 67, 68, 69, 70, 71] The interaction energy between two molecules can be partitioned into various components, including charge transfer (CT). The magnitudes of these components are dependent upon how the partitioning is done, with interaction energy contributing around 10% or less[67, 71] to the binding energy.[63, 68] A number of methods find that the CT contribution to the energy is around 20% to 40%.[64, 65, 66, 67, 69, 70] In the minimum-energy-hydrogen-bonded configuration of the water dimer, one molecule acts as a hydrogen bond donor and the other as an acceptor. Asymmetry between the molecules leads to a transfer of charge from the hydrogen acceptor to the donor.[67, 72] The amount of charge transferred between the two water molecules is small, around -0.02 e[67, 68, 70, 72, 73], depending on the method of partitioning the electronic density utilized.[67, 70] Electronic structure calculations also indicate

This chapter has been published previously as a paper in the *Journal of Chemical Physics*, *134*, 184507 (2011): "The effects of charge transfer on the properties of liquid water."

that charge transfer is present in solute-water interactions.[74, 75, 76, 77, 78] Experimentally, charge transfer between hydrogen-bonded molecules may be indicated by the red shift in OH stretching frequencies.[79, 80, 81] Additional experimental evidence of charge transfer comes from integration of electron densities from X-ray diffraction, which can lead to molecules with non-integral charges.[82, 83] In one notable case, half an electron is transferred from one molecular ion to another.[82] For water in hydrates, the molecular charges are small, but non-zero.[83] The importance of charge-transfer is indicated in the results of X-ray absorption spectroscopy for water-ion interactions[47] and in molecular-beam scattering experiments for rare gas and H_2 interactions with water.[84, 85, 86]

Despite the experimental and *ab initio* results demonstrating the importance of charge transfer, there have only been a few interaction potentials developed for water and other hydrogen-bonding molecules which include charge transfer.[79, 87, 88, 89, 90, 91, 92, 93, 94] These models, often fairly complex, have been primarily applied to the water dimer or water clusters.[79, 88, 91, 92, 93, 94] Some of these models include a charge-transfer term in the energy, but do not actually transfer any charge, so that the molecules remain neutral, and the Coulombic interactions are not affected by the charge-transfer interactions.[88, 90, 94] Other potentials with charge transfer are reactive models, which can include charge transfer effects as bonds are broken.[87, 89] In the case of ionic liquids, an approach to handling CT includes assigning non-integer charges to the ions.[95, 96] The number of studies of charge transfer pales in comparison to the large number of polarizable potentials developed for water[7, 97, 98, 99, 100, 101, 102, 103, 104, 105, 106, 107, 108, 109, 110, 111, 112, 113, 114, 115, 116] or the re-parameterizations of existing non-polarizable models.[2, 3, 61, 117, 118, 119, 120, 121, 122] Charge transfer is included in *ab initio* molecular dynamics simulations, but implementation of these methods can be limited by system size and timescales. It is desirable to have simpler, faster models for many applications.

The success of both the non-polarizable and polarizable models without charge transfer in reproducing many of the properties of water suggests a contradiction with the *ab initio*

results for water dimers and clusters, which indicate the importance of charge transfer. A question as to whether the success of the water potentials is simply fortuitous follows from these data.[70] In this chapter, a new method of treating charge transfer, which can be easily added to existing potentials, is presented. Two water potentials are presented, one polarizable and one non-polarizable, utilizing this new CT method. The effects of charge transfer on the properties of bulk water are examined.

3.2 Methods

Charge transfer is introduced by adding a fixed amount of charge for each hydrogen bond formed by the molecule. This results in a discrete amount of charge, δQ_t, transferred from the hydrogen-bond acceptor to the hydrogen-bond donor. Hydrogen bonds are defined as being made if the distance between a hydrogen and oxygen atom is less than a distance r_1. In order to smoothly turn off charge transfer as a pair of water molecules moves apart, the hydrogen bond definition switches from 1 to 0 over a range from r_1 to r_2 according to

$$N(iO\cdots j\alpha) = \begin{cases} 1 & r_{iOj\alpha} < r_1 \\ (1/2)[1+\cos(\pi(r_{iOj\alpha}-r_1)/(r_2-r_1))] & r_1 < r_{iOj\alpha} < r_2 \\ 0 & r_2 < r_{iOj\alpha} \end{cases} , \qquad (3.1)$$

where $r_{iOj\alpha}$ is the distance between the oxygen on molecule i and a hydrogen (α) on molecule j. N($iO\cdots j\alpha$) indicates the hydrogen bond formed between atoms iO and $j\alpha$, with molecule j as the hydrogen-bond donor. The values of r_1 and r_2 are taken to be 2.3 and 2.8 Å, which corresponds to the first minimum in the oxygen-hydrogen pair correlation function. Beyond a value of 2.8 Å, electronic structure methods find that there is essentially no charge transfer.[72] The total number of hydrogen bonds molecule i makes as an acceptor is given by

$$N_a^i = \sum_{j\neq i} \sum_{\alpha=1,2} N(iO\cdots j\alpha)\,, \qquad (3.2)$$

where the sum over α is the sum over the two hydrogens on molecule j. The total number of hydrogen bonds molecule i makes as a donor is given by

$$N_d^i = \sum_{j \neq i} \sum_{\alpha=1,2} N(jO \cdots i\alpha) \,, \tag{3.3}$$

where this sum over α is over the two hydrogen atoms on molecule i. The total charge of a molecule is given by the difference between the number of hydrogen bonds the molecule makes as a donor and as an acceptor, through

$$Q_t^i = (N_d^i - N_a^i)\delta Q_t. \tag{3.4}$$

Note that N_d^i and N_a^i do not have to be integers.

The charge transfer from the HB acceptor to the donor[67, 72] weakens the electrostatic interaction between the two molecules by giving the oxygen atom a smaller negative charge. The gain in energy from charge transfer is, therefore, not due to increased electrostatic interactions, but due to an electronegativity difference. The donating water in a hydrogen bond is more electronegative than the molecule which accepts, perhaps because the electrons around that oxygen are less confined.[67] The energetic contribution of charge transfer is included as

$$E_{CT}(\delta Q_t) = \mu_{CT}\delta Q_t + (1/2)\eta_{CT}\delta Q_t^2 \,, \tag{3.5}$$

where μ_{CT} and η_{CT} are the first- and second-order contributions to the energy as a function of charge transfer (the chemical potential and hardness parameters, respectively) and can be taken from the electronic structure calculations of Korchowiec and Uchimaru.[67] Using those values (μ_{CT}=10.67 kcal/mol/e and η_{CT}= 308.11 kcal/mol/e) and δQ_t= -0.02 e gives a charge transfer energy of -0.15 kcal/mol for each hydrogen bond. This is a formalism for treating charge transfer called DCT, which can be added to existing force fields. Our approach is added to both standard non-polarizable and polarizable water models, as described in the following sections.

I. Charge transfer in non-polarizable models. The total molecular charge is determined by the number hydrogen bonds the molecule makes, calculated by Equation 3.4. The procedure for distributing that charge among the atoms of the molecule needs to be determined. There are a number of different possibilities. The excess charge could be distributed equally among all the atoms or just given to the oxygen atom. The charge increments for each atom and the total amount of charge transferred could also be considered as adjustable parameters of the model. We chose to use the results of electronic structure calculations of Gálvez, Gómez and Pacios for the water dimer.[72] That study, using an Atoms in Molecules (AIM) method to partition the charge, found that there is a substantial redistribution of charge that goes along with charge transfer. Their results show that for a charge transfer of about -0.02 e, the oxygen on the molecule donating the hydrogen bond is about 0.03 e more negative than the accepting oxygen. The balance of the charge gets redistributed among the hydrogen atoms. This is the basis for how the transferred charge redistributes in our model, as shown by

$$\begin{gathered} H-O-H\cdots\cdots O-H_2 \\ (-0.01)\,(-0.02)\,(0.01) \qquad (0.01)\,(0.005,\,0.005)\,, \end{gathered}$$

where the numbers below each atom indicate the change in the charge of that atom in e. The total charge for each atom is found from

$$\begin{pmatrix} q_{iO} \\ q_{iH1} \\ q_{iH2} \end{pmatrix} = \begin{pmatrix} -2q_H \\ q_H \\ q_H \end{pmatrix} + \begin{pmatrix} -0.02 & -0.02 & 0.01 \\ 0.01 & -0.01 & 0.005 \\ -0.01 & 0.01 & 0.005 \end{pmatrix} \begin{pmatrix} N_d^{i1} \\ N_d^{i2} \\ N_a^{i} \end{pmatrix}, \tag{3.6}$$

where q_H is the hydrogen atom charge for a molecule without hydrogen bonds. The total number of hydrogen bonds formed by molecule i involving hydrogen atom α is given by

$$N_d^{i\alpha} = \sum_{j \neq i} N(jO \cdots i\alpha). \tag{3.7}$$

The charge transfer given by Eq. 3.6 redistributes charge among atoms on the same molecule, as well as transfers charge between molecules, resulting in a net change in the charges between a molecule with 0 and with 4 hydrogen bonds. This change for the hydrogen atom is equal to 0.01 e, giving a small increase (0.04 Debye) in the dipole moment.

A number of non-polarizable potentials add a polarization energy to the potential energy.[2, 3, 61, 117] The charges of most water models are enhanced from the gas phase values, representative of charges that are polarized by their environment. The energy required for this is

$$E_{pol} = (\mu - \mu_{gp})^2/(2\alpha)\,, \tag{3.8}$$

where μ is the model's dipole moment, μ_{gp} is the gas-phase dipole moment, and α is the polarizability. Adding this constant term to the energy leads to models with stronger interaction energies, which tends to lead to better reproduction of the properties of water.[2, 3, 61] We add this term to the charge transfer water model, as well. In this case, the polarization energy is not a constant because μ is coupled to charge transfer.

The interaction energy between two molecules i and j is given by a sum of Lennard-Jones interactions between oxygen atoms and Coulombic interactions between the charge sites plus the charge transfer and polarization energies from Equations 3.5 and 3.8. The energy for N water molecules is given by

$$E = \sum_{i=1}^{N-1}\sum_{j>i}\left(4\epsilon\left[\left(\frac{\sigma}{r_{iOjO}}\right)^{12} - \left(\frac{\sigma}{r_{iOjO}}\right)^{6}\right] + \sum_{\alpha\beta}\frac{q_{i\alpha}q_{j\beta}}{r_{i\alpha j\beta}}\right)$$

$$+ \sum_{i=1}^{N}(\mu_i - \mu_{gp})^2/(2\alpha) + \mu_{CT}(N_d^i\delta Q_t) + (1/2)\eta_{CT}(N_d^i\delta Q_t)^2, \tag{3.9}$$

where r_{iOjO} is the distance between the two oxygen atoms, and the sum of α and β is over the charge sites on the two molecules. Further details about implementing the method are given in the appendix.

This method could be easily combined with methods for polarizability, like point inducible dipoles[97, 98, 99, 101, 102, 103, 105, 106, 107, 109, 110, 113] and Drude oscillators[114, 115, 116], which do not involve molecular charges in the polarization response. A model with both charge transfer and polarization is described next.

II. Charge transfer in fluctuating charge models. In fluctuating charge models, the charges are variables, which are determined by minimizing the energy subject to a constraint. In most fluctuating charge water models, a constraint of charge neutrality is put on each molecule.[7, 111, 112] In our charge transfer formalism, the constraint on each molecule will be determined by Equation 3.4. The energy has the intermolecular Coulombic and Lennard-Jones terms, plus an intramolecular Taylor series expansion in charge variables, to give

$$x = \left(E = \sum_{i=1}^{N-1} \sum_{j>i} \left(4\epsilon \left[\left(\frac{\sigma}{r_{iOjO}} \right)^{12} - \left(\frac{\sigma}{r_{iOjO}} \right)^{6} \right] + \sum_{\alpha\beta} \frac{q_{i\alpha} q_{j\beta}}{r_{i\alpha j\beta}} \right) \right.$$
$$\left. + \sum_{i=1}^{N} \left(\mu_{CT}(N_d^i \delta Q_t) + (1/2)\eta_{CT}(N_d^i \delta Q_t)^2 + \sum_{\alpha} \tilde{\chi}_{\alpha}^0 q_{i\alpha} + \frac{1}{2} \sum_{\alpha} \sum_{\beta} q_{i\alpha} q_{i\beta} J_{\alpha\beta}(r_{i\alpha i\beta}) - E_i^{gp} \right) \right. \tag{3.10}$$

$$\left. - \sum_{1=1}^{N} \lambda_i \left(\sum_{\alpha} q_{i\alpha} - Q_t^i \right) \right) , \tag{3.11}$$

where we have added the charge transfer energy, the energy of an isolated or gas-phase molecule is E_i^{gp}, and $\tilde{\chi}_{\alpha}^0$ and $J_{\alpha\beta}(r_{i\alpha,i\beta})$ are parameters of the potential that depend on atom types. Following earlier work[7, 123], the interaction for intramolecular pairs is given by the Coulomb overlap integral,

$$J_{\alpha\beta}(r_{i\alpha i\beta}) = \int dr_{i\alpha} dr_{i\beta} |\phi_{n_\alpha}(r_{i\alpha})|^2 \frac{1}{|r_{i\alpha} - r_{i\beta} - r|} |\phi_{n_\beta}(r_{i\beta})|^2 , \tag{3.12}$$

between Slater functions,

$$\phi_\alpha(r) = A_{n_\alpha} r^{n_\alpha - 1} e^{-\zeta_\alpha r} , \tag{3.13}$$

where A_{n_α} is a normalization constant, n_α is the principal quantum number of atom α, and the exponent, ζ_α, is taken to be an adjustable parameter. The self-term, $J_{\alpha\alpha}(0)$, is also determined by the ζ_α parameter. For hydrogen atoms, with n_α=1, we have $J_{\alpha\alpha}(0)=\frac{5}{8}\zeta_\alpha$. For oxygen atoms, with n_α=2, we have $J_{\alpha\alpha}(0)=\frac{93}{256}\zeta_\alpha$. The last term in Equation 3.11 represents the charge constraint on each molecule enforced using an undetermined multiplier, λ_i. The only differences from the original fluctuating charge models are the charge transfer energy and the value of the charge constraint for each molecule. In the appendix, additional details are given regarding implementation of this method in molecular dynamics simulations.

Charge transfer can be included using a fluctuating charge formalism by simply changing the charge constraint.[7] This can lead to unphysical behavior.[7, 91, 92, 124] The system becomes conductive when charge transfer is allowed among all molecules. Unphysical characteristics arise when charge transfer occurs over large distances and when charge is transferred in the wrong direction, from the hydrogen bond donor to the acceptor. A number of methods have been developed to address these problems, based on variations of atom-atom charge transfer or bond charge increment models.[91, 92, 124, 125, 126] In these models, the fluctuating charge variables are taken to be the charge difference between bonded atoms, rather than atomic charges. This provides a convenient formalism for controlling the amount of charge flow between molecules. The DCT approach developed here was designed to be simple to implement, compatible with different types of force fields, and capable of satisfying the following physical requirements: no long-range charge transfer, not conductive, and correct amount and direction of charge transfer.

Parameter Optimization. The objective is to develop potentials that are accurate for the liquid phase, particularly near 298 K and at a pressure of 1 atm. For both models, we use the TIP4P geometry, with r_{OH}=0.9572 Å, θ_{HOH}=104.52° and an M-site position, δ_M=0.150 Å. The Lennard-Jones 12-6 form is assumed and other variations, like a softer repulsive potential, were not explored. The charge transfer amount of -0.02 e, a value consistent with a number of studies [67, 68, 70, 72, 73], the μ_{CT} and η_{CT} parameters in E_{CT}

(taken from Ref. [67]), and the charge redistribution for the TIP4P-DCT model (given by Eq. 3.6) were not treated as variational parameters. This leaves three parameters for the TIP4P+DCT model (the Lennard-Jones ϵ and σ parameters and a charge parameter q_H) and five parameters for the TIP4P-FQ+DCT model. The TIP4P-FQ+DCT model parameters are ϵ, σ, $\tilde{\chi}_O^0 - \tilde{\chi}_H^0$ (only the difference in $\tilde{\chi}_\alpha^0$ between the oxygen and hydrogen atoms types is significant), and the two Slater exponents, ζ_O and ζ_H, which determine the second order coefficients, $J_{\alpha\beta}$. As in the original TIP4P-FQ model, the model will be parameterized to give the correct gas-phase dipole moment (1.85 Debye[127]). This condition eliminates $\tilde{\chi}_O^0 - \tilde{\chi}_H^0$ as an adjustable parameter, as there is only one value for a ζ_O and ζ_H pair that gives the correct gas-phase dipole moment. The four remaining parameters were chosen to optimize various properties of liquid water at 298 K and 1 atm: density, energy, dielectric constant, translational diffusion constant, and oxygen-oxygen pair correlation function. For the TIP4P+DCT model, the three parameters were optimized against the same properties at 298 K and also chosen to reproduce the liquid density as a function of temperature over the range of 260 to 310 K.

Simulation Details. All MD simulations were conducted using our own programs for the two charge transfer potentials. The simulations were performed in both the TPN and TVN ensembles with a 1 femtosecond timestep using the Verlet algorithm and 256 water molecules. Temperature was controlled by a Nosé-Hoover thermostat. For the TIP4P-FQ+DCT model, charges were treated as dynamical variables, assigned fictitious masses, and propagated with extended Lagrangian formalism, as described in the previous section. Ewald summations were used to calculate the electrostatic interactions. Note that other water models have been parameterized to be used with various truncation methods[2, 3], and using different truncation methods can alter the results. In this work, no truncations, switching functions, or long-range corrections are used, and interactions between all nearest image particles are calculated. Each temperature was simulated for at least 3 ns to generate equilibrium properties. The TPN simulations were done at a pressure of 1 atm. For dynam-

ical properties, TVN simulations were used and data was gathered from 20 different 10 ps simulations. To check if the inclusion of charge transfer and the switching function defined by Eq. 3.1 influences the integration of the equations of motion, we monitored the energy conservation of the models. Energy conservation was monitored through

$$\Delta E = \langle (E(t) - E(0)) \rangle / \langle |E| \rangle \, , \tag{3.14}$$

where $\langle (E(t) - E(0)) \rangle$ is the difference in the total energy at the start of the simulation and a later time, t (using $t = 100$ ps). The average magnitude of the energy is $\langle |E| \rangle$. In our implementation of molecular dynamics, ΔE is 0.0011±0.0003, 0.0007±0.0004, 0.0011±0.003, and 0.0007±0.0004 for TIP4P, TIP4P-FQ, TIP4P+DCT, and TIP4P-FQ+DCT, respectively. These results show that charge transfer does not lead to any additional loss of energy conservation in the dynamics than non-charge-transfer models.

3.3 Results and Discussion

The parameters for the two DCT models are given on Tables 3.1 and 3.2, along with parameters for other models. The properties of the two models for the liquid at a temperature of 298 K and atmospheric pressure are given in Table 3.4, all calculated using the standard formulas (as described in Reference [121]). Previously-calculated properties

Table 3.1: Parameters for the TIP4P-DCT, TIP4P[6], TIP4P/2005[2] and TIP4P-Ew[3] models.

Model	ϵ (kcal/mol)	σ (Å)	q_H (e) (e)	δ_M (Å)
TIP4P+DCT	0.1709	3.177	0.5360	0.150
TIP4P	0.1550	3.154	0.520	0.150
TIP4P/2005	0.1852	3.1589	0.5564	0.1546
TIP4P-Ew	0.162750	3.16435	0.52422	0.125

of other polarizable and non-polarizable models and experimental values are also shown. At this state, all models tend to give accurate properties (particularly the energy and density)

Table 3.2: Parameters for the TIP4P-FQ+DCT and TIP4P-FQ[7] models.

Model	ϵ (kcal/mol)	σ (Å)	$\tilde{\chi}^0_O - \tilde{\chi}^0_H$ [kcal/(mol e)]	ζ_H (Å^{-1})	ζ_O (Å^{-1})	δ_M (Å)
TIP4P-FQ+DCT	0.2633	3.171	70.80	1.776	3.099	1.50
TIP4P-FQ	0.2862	3.159	68.49	1.701	3.080	1.50

by construction. Both charge transfer models give results comparable to the best of the water models. The oxygen-oxygen radial distribution functions for TIP4P+DCT and TIP4P-FQ+DCT are shown in Figure 3.1. The first peak is slightly

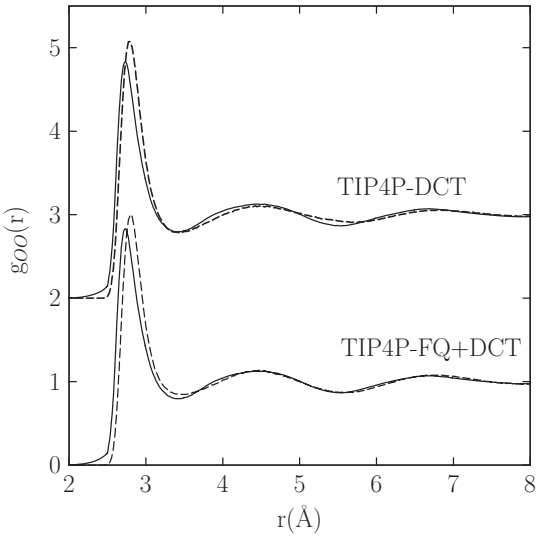

Figure 3.1: The oxygen-oxygen pair correlation function for the TIP4P+DCT and TIP4P-FQ+DCT potentials (dashed lines) and X-ray experimental data (solid line).[1] The correlation function for the TIP4P+DCT model has been shifted by 2 units.

high with a larger separation than other models give[2, 3, 6, 7], but the agreement is good with experiment[1] for both models.

The dielectric constant for the TIP4P+DCT model is about the same as the TIP4P-type models with no charge transfer. Attempts to improve the dielectric constant by increasing the charges led to a significant decrease in the quality of the model in terms of other properties. Perhaps by changing the position of the M-site, a model with a better dielectric constant could result, as is suggested in the comparison between TIP4P/2005 and TIP4P-

Ew. Most non-polarizable models underestimate the liquid dielectric constant, except for TIP5P[129], TIP5P-E[121], and TIP3P.[6] This may be related to the low quadrupole moments found for those three models.[121] Non-polarizable models give dielectric constants for ice I_h that are too low, as well.[131, 132] The TIP4P-FQ+DCT model was made to have an accurate dielectric constant by reducing the polarizability. The DCT polarizable model is less polarizable than the original TIP4P-FQ model, with values for the polarizability tensor equal to α_{zz}=0.79 Å^3 and α_{yy}=2.34 Å^3 compared to α_{zz}=0.82 Å^3 and α_{yy}=2.55 Å^3 for TIP4P-FQ.[7] The molecule is considered to be in the zy-plane with the dipole, C_2, axis in the z-direction. (For both models, which do not have polarization response out of the plane of the molecule, α_{xx}=0.) Experimentally, all components are roughly 1.5 Å^3.[133] The smaller polarizability leads to a slightly smaller liquid-phase dipole moment (2.596 Debye, see Table 3.3) than the TIP4P model (2.62 Debye).[7]

Table 3.3: Average values for the magnitude of the total charge, dipole moment and quadrupole moments of liquid water at a temperature of 298 K and a pressure of 1 atm.

Model	$\langle\lvert Q_{tot}\rvert\rangle$ (e)	μ (Debye)	Q_{xx} (Debye·Å)	Q_{yy} (Debye·Å)	Q_{zz} (Debye·Å)
TIP4P+DCT	0.00799	2.288	-2.196	2.316	-0.120
TIP4P-FQ+DCT	0.00774	2.596	-2.472	2.608	-0.135

The optical dielectric constant, ϵ_∞, for the TIP4P+DCT model equals 1 because it is not a polarizable model. For the TIP4P-FQ+DCT model, ϵ_∞ is 1.540±0.002, smaller than the value for the TIP4P-FQ model (1.592)[7] and the experimental value (1.79).[134] Two notable differences between the models with and without charge transfer are the heat capacity, C_p, and the coefficient of thermal expansion, α_p. Both properties are smaller for the charge transfer models than a corresponding model without charge transfer, as seen by a comparison of the TIP4P+DCT and TIP4P, TIP4P-Ew, and TIP4P/2005 models and of the TIP4P-FQ+DCT and TIP4P-FQ models. Charge transfer acts to reduce the change in the energy and density with temperature. The density as a function of temperature is shown in Figure 3.2 (see also Table 3.5). Both charge transfer models show a density

Table 3.4: Properties of selected water models at T = 298 K and P = 1 atm. density, ρ, average potential energy per molecule, E, isothermal compressibility, κ_T, coefficient of thermal expansion, α_p, constant pressure heat capacity, C_p, dielectric constant, ϵ, and translational diffusion constant D, compared to experimental values.[5, 8, 9, 10, 11]

Model	ρ (g/cm^3)	E (kcal/mol)	κ_T (10^{-6} bar^{-1})	α_p ($10^5 K^{-1}$)	C_p (cal $mol^{-1}K^{-1}$)	ϵ	D ($10^{-9}m^2/s$)
TIP4P+DCT	0.9977±0.0008	-10.185±0.003	50±1	25±3	14.4±0.2	58±2	2.4±0.1
TIP4P-FQ+DCT	0.9968±0.0006	-9.941±0.005	40±1	44±5	22.6±0.5	78±2	1.9±0.1
TIP4P[118, 128]	1.001	-10.1	60±5	44±8	20	60±10	3.3
TIP4P-Ew[3]	0.9954	-9.99	48.1	32	19.2	63.9±0.9	2.321
TIP4P/2005[2]	0.9979	-10.30	46.5	28	18.9	60	2.08
TIP5P[129]	0.999	-9.87	41±2	63±6	29	82±2	2.6
TIP4P-FQ[4, 7]	0.998±1	-9.92±1	38±2	63±8	25.0±0.6	79±8	1.9±0.1
SWM4+DP[114]	0.999	-9.927				79±5	2.30±0.04
AMOEBA[113, 130]	1.0004±0.0009	-9.89±0.08			21.3	82±13	2.02±0.005
Experiment	0.9971	-9.92	45.8	25.6	18.0	78.4	2.27

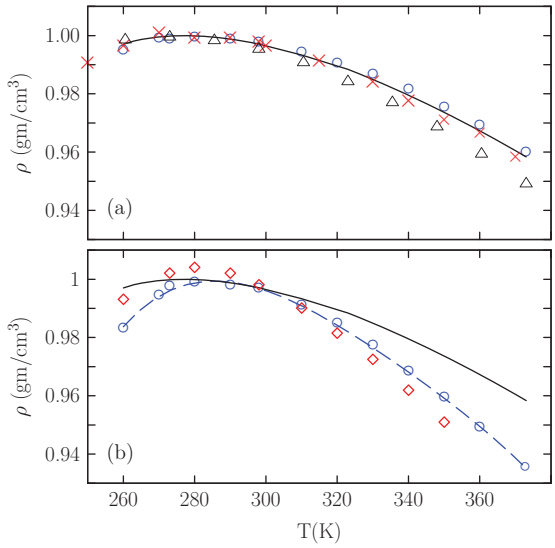

Figure 3.2: Density of (a) TIP4P+DCT (circles), TIP4P/2005[2](crosses), and TIP4P-Ew[3](triangles) and (b) TIP4P-FQ+DCT (circles and dashed line) and TIP4P-FQ[4] (diamonds) compared to Experiment[5](solid line).

Table 3.5: Liquid densities at a pressure of 1 atm, compared to experiment.[5]

T (K)	Density (g/cm^3)		
	TIP4P+DCT	TIP4P-FQ+DCT	Experiment
260	0.9951 ± 0.0009	0.9823 ± 0.0024	0.9970
270	0.9989 ± 0.0008	0.9943 ± 0.0014	0.9995
273	0.9988 ± 0.0009	0.9977 ± 0.0014	0.9998
280	0.9996 ± 0.0005	0.9988 ± 0.0013	0.9999
290	0.9989 ± 0.0008	0.9979 ± 0.0013	0.9988
298	0.9977 ± 0.0008	0.9968 ± 0.0006	0.9971
310	0.9942 ± 0.0008	0.9910 ± 0.0007	0.9933
320	0.9906 ± 0.0008	0.9847 ± 0.0008	0.9884
330	0.9868 ± 0.0005	0.9772 ± 0.0003	0.9848
340	0.9815 ± 0.0005	0.9682 ± 0.0004	0.9795
350	0.9753 ± 0.0005	0.9593 ± 0.0005	0.9737
360	0.9693 ± 0.0005	0.9491 ± 0.0003	0.9673
373	0.9598 ± 0.0005	0.9357 ± 0.0004	0.9584

maximum near the experimental value of 281 K.[5] The TIP4P+DCT model is very accurate over the whole range of temperatures for which the liquid is stable. Also shown in Figure 3.2(a) are the results for the TIP4P-Ew and TIP4P/2005 models – two of the models which best reproduce the liquid density over this temperature range and give a value of α_p closest to experiment. The TIP4P-FQ+DCT model gives an improvement over the TIP4P-FQ model for the density at higher temperatures and near the density maximum. In addition to the TIP4P-Ew, TIP4P/2005, and TIP4P-FQ models, a number of water models give a temperature of maximum density (TMD) near 281 K, including TIP5P[129], TIP5P-E[121], AMOEBA[130], the 6-site Nada and van der Eerden model[135], PPC[108], BSV[136], and TIP4P-Pol2.[111] Many of these models, like TIP4P+DCT, were optimized to reproduce this property.[2, 3, 121, 129, 135] Many commonly-used models do not have a TMD above 250K or a TMD not close to 277 K including TIP4P, TIP3P, SPC,[137] and SPC/E.[138, 139] Interestingly, all these models tend to overestimate α_p, giving a density that changes too much with temperature, even those with fairly accurate TMD values. The TIP4P/2005 and AMOEBA models give a temperature dependence closest to experiment, along with TIP4P+DCT.

The average charge on a molecule, $\langle|Q_{tot}|\rangle$, in the room temperature liquid is about 0.008 e (see Table 3.3), as given by both charge transfer models, which is less than the models give for the hydrogen bonded dimer (0.020 e). On average, there is less overall charge transfer for a water molecule in the bulk liquid than there is for the dimer. Charge transfer occurs for the hydrogen-bonded dimer because there is asymmetry between the two molecules as one donates and one accepts a hydrogen bond. In the liquid, each molecule is in a more symmetric local environment. Fluctuations in the liquid structure give rise to configurations in which a molecule has an unequal number of donor and acceptor hydrogen bonds. The distribution of the difference between the hydrogen bonds a molecule makes as a donor and as an acceptor is shown in Figure 3.3 for three different temperatures using the TIP4P+DCT potential. Here we are defining a hydrogen bond as existing if the O$\cdots$H

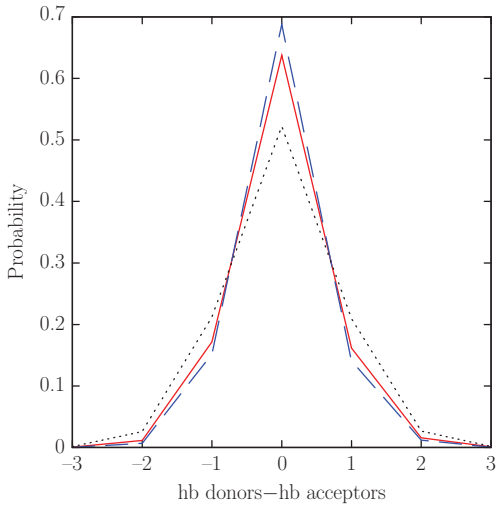

Figure 3.3: Probability distribution of the difference in the number of hydrogen bonds a molecule forms as a donor and as an acceptor at three different temperatures, 273 K (dashed line), 298 K (solid line), and 373 K (dotted line)
from the TIP4P+DCT potential.

distance between two molecules is less than 2.55 Å, which is half the distance between r_1 and r_2. (See Equation 3.1.) Most molecules (about 0.64 or a little less than 2/3 at 298 K) form an equal number of donor and acceptor hydrogen bonds. Those molecules would be given a charge of zero by the DCT models. Only a minority of molecules (a little more than 1/3 at 298 K) have a charge. As the temperature increases, the hydrogen bond distribution gets wider, more water molecules have an asymmetric hydrogen bond structure, and $\langle|Q_{tot}|\rangle$ increases. At 273 K, $\langle|Q_{tot}|\rangle$ is 0.0068 e. With a temperature rise to 373 K, $\langle|Q_{tot}|\rangle$ increases to 0.0103 e. The results are similar for the TIP4P-FQ+DCT model.

3.4 Conclusion

Our new method for treating charge transfer, DCT, has been presented. The method is general enough that it can be added to a variety of potentials, which we demonstrated by combining it with both a polarizable and a non-polarizable model. The method is simple to implement and, because charge transfer is determined from local geometry only, finding the charge of a molecule does not require minimizing an energy or solving a self-consistent

set of equations by iteration or other methods. DCT can be constructed to give physically reasonable amounts of charge transfer without giving rise to unphysical behavior, such as transferring charge at large distances or becoming conductive. For the parameterization process, much in the same way molecular charges for a model can be found from electronic structure calculations, the change in the charges due to the formation of a dimer or larger cluster can be used to determine the charge transfer part of the potential. In this implementation, charge is only transferred as a result of hydrogen bonds, as is indicated from calculations of the dimer.[62, 63, 64, 65, 66, 67, 68, 69, 70, 71] While hydrogen bonds are likely to be the most significant influence on charge transfer for a molecule in the liquid, other factors like local density fluctuations may influence charge transfer, as well. Examining the results of *ab initio* MD could lead to improved models for charge transfer.

Both charge transfer models accurately reproduce structural, dynamical, and thermodynamic properties of liquid water. The accuracy of these models compare well to some of the best polarizable (including TIP4P-FQ[7], SWM4+DP[114], AMEOBA[113]) and non-polarizable (TIP4P-Ew[3], TIP4P/2005[2]) water models. A notable difference between the models with charge transfer and those without is that charge transfer, as implemented here, decreases the heat capacity and the temperature dependence of the density relative to other classical potentials. The charge transfer energy has its own temperature dependence due to structural changes in the liquid. This reduces the energy increase and the decrease in the density with temperature.

The total amount of charge transferred to a water molecule in the liquid is only about 0.008 e, at 298 K, which is less than the amount of charge transfer for the dimer (0.020 e). In the liquid, a water molecule is in a symmetric environment, on average, donating and accepting an equal amount of hydrogen bonds. About a third of the time, a molecule donates more or less, hydrogen bonds than it accepts (see Fig. 3.3), with this fraction being temperature dependent. The net charge will be zero for most of the molecules. Note that the change in going from the dimer to the liquid is different from the effects of polarizability,

which increase rather than decrease as the symmetry of neighboring molecules combine to enhance the electric field and increase the dipole moment. The symmetry of the charge transfer interactions in the liquid is the suggested reason for the success of models without charge transfer, despite the importance of charge transfer for the dimer, a question raised in the Introduction, and elsewhere.[70] If symmetry is broken by the addition of a solute or the creation of an interface, then charge transfer would become more important. Charge transfer then could make a more significant contribution to the properties of water as a solvent than as a pure liquid.

Acknowledgements This work was supported from the National Science Foundation under contract number CHE-0611679. AJL gratefully acknowledges support from the State of Louisiana Board of Regents. We would like to thank Steve Stuart and Tom Beck for helpful discussions.

Chapter 4

Charge Transfer at Aqueous Interfaces

4.1 Charge Transfer at the Liquid/Vapor Interface

4.1.1 Introduction

Properties of the air/water interface differ greatly from bulk water properties. The local hydrogen-bonding structure, orientational ordering, electrochemical properties, and other properties uniquely characterize the surface. Extensive experimental and computational data supporting these differing surface properties have been reported.[51, 140, 141, 142, 143, 144, 145, 146, 147, 148, 149, 150, 151, 152] Though there are innumerable water potentials in use today, not all potentials are equal in accuracy, efficiency, or complexity. A more sophisticated model may include many-body electrostatic effects, such as polarization and charge transfer, which make significant contributions to the behavior of molecules and intermolecular interactions.[7, 110, 153]

In environments of high local asymmetry, many-body effects become more pronounced. The dielectric constants, as an example, of air and water are dramatically different. Therefore, at the interface of air and water, the electrostatic environment will vary greatly from the situation in the bulk water. When there is high hydrogen bond symmetry, molecules of the TIP4P+DCT and TIP4P-FQ+DCT models have no charge. However, when the sym-

The work on the liquid/vapor interface is a collaborative effort with Collin D. Wick, Louisiana Tech, Rustin, LA. *Manuscript in preparation.*

metry is broken at the surface, a small negative charge is seen.[24] Evidence of this effect, the negative surface charge, has been observed experimentally. [150, 154, 155, 156, 157, 158] Models without many-body effects can reproduce the results of those with the effects included because of this symmetry issue. Computational studies have even shown the electrostatic potential across the surface is similar for models with and without many-body effects included.[144, 159, 160, 161, 162]

A phenomenon seen only in water potentials equipped with many-body interactions is expansion of the liquid water at the surface. Polarizability and charge transfer have the effect of weakening the interactions, mitigating the dipoles of the molecules at the air/water interface, causing the HB network to expand. Models that do not include these interactions, even flexible models, do not exhibit this surface effect.[140, 142, 163] Polarizability has been shown to affect the behavior of ions and their preference for the surface. Large, polarizable anions tend to prefer the surface, whereas smaller, less polarizable ions prefer to be buried in the bulk. [43, 160, 164]

The most-commonly neglected of all intermolecular interactions is charge transfer (CT). Charge transfer is the redistribution of electron density between two particles involved in a non-covalent interaction. Electronic structure calculations have shown that CT is significant in the interactions between water and both charged and neutral solutes.[12] With respect to water, a transfer of charge occurs when forming a hydrogen bond. A small amount of charge is transferred from the HB acceptor back to the HB donor molecule.[67, 68, 70, 72, 73] The asymmetrical hydrogen-bonding structure of the air/water interface lends itself to a more pronounced effect from these many-body interactions.[143]

Experimental data indicating a negative surface charge at the air/water interface[150, 154, 155, 156, 157, 158] may be explained by an aggregation of hydroxide at the surface. A few *ab initio* molecular dynamics (AIMD) potentials explicitly include charge transfer.[140, 141, 165] None of the studies conducted, however, investigate the specific role of charge transfer in the intermolecular interaction potential. In this study, the the role of intermolecular charge

transfer at the interface of neat water and vapor is investigated. Rigid water molecules with and without charge transfer and flexible and polarizable water models are utilized.

Potentials Under Study

Three classes of molecular models were implemented in the investigation of charge transfer at the air/water interface. One is based on a rigid structure with fixed charges, the TIP4P water model[6]. The second is the fluctuating charge version of TIP4P (TIP4P-FQ)[123]. The third is based on a recently-developed flexible and polarizable water model (FLEX).[166] The models, TIP4P+DCT and TIP4P-FQ+DCT, of Lee and Rick (2011)[24] are outlined in detail in Chapter 3. The FLEX model[166] of Collin Wick (2012) is a flexible, polarizable water potential with water structure similar to that of TIP4P with an added flexibility component. Rather than intramolecular charge transfer, a single-point polarizability of 1.444 Å^{-1} is located on the M-site. Details of the bond-stretching and bond-bending potentials are described in Reference [166]. The M-site position changes with the geometry of the water molecule according to

$$x_M = \gamma(x_{H1} + x_{H2}) + (1 - 2\gamma)x_0 \,, \tag{4.1}$$

where γ was set to 0.182. The intramolecular charge distribution is also dependent upon geometry. The oxygen-hydrogen intramolecular bond length (r^0_{OH}) and H–O–H bond angle (θ_{HOH}) in

$$q^0_H = -0.14 r^0_{OH} + 0.14\theta_{HOH} + 0.398 \tag{4.2}$$

were parameterized to agree with the experimental liquid and gas phase values for water geometry.[167] The FLEX oxygen charge is the negative of the sum of the two hydrogen charges. The van der Waals and repulsion interactions are treated using the Buckingham exponential-6 potential,

$$U_{vdw} = \epsilon \left[\frac{6}{\lambda} exp\left(\lambda\left[1 - \frac{r}{\sigma}\right]\right) - \left(\frac{\sigma}{r}\right)^6 \right] . \tag{4.3}$$

The values used were 3.685 Å, 0.16 kcal/mol, and 13.5 for σ, ϵ, and λ, respectively. Wick's model, CT-FLEX, incorporates charge transfer. The σ value for CT-FLEX was set to 3.67 Å, with all other parameters as stated. Electrostatic interactions for sites with a distance less than 5 Å are damped with respect to standard Coulombic interaction to account for the effects that arise due to the Pauli Exclusion Principle.[168, 169] Dipoles were induced from the polarizabilities based on their local electric fields, creating a many-body situation similar to that of the TIP4P-FQ model. The FLEX model requires a much smaller timestep than that of TIP4P and TIP4P-FQ (0.2 fs versus 1–2 fs) to describe its faster vibrational modes. It should be noted that multiple timestep MD cannot be used because the fast modes are coupled to molecular charge through Equation 4.2, and consequently, to intermolecular interactions. The electrostatics are described using the predictor corrector algorithm.[170]

Treating Intermolecular Charge Transfer

Charge transfer between neighboring water molecules depends on their O$\cdots$H distance (r_{OH}). The distance-dependent functions that determine the amount of charge transfer smoothly go from 0 to 1 as r_{OH} becomes smaller are

$$N = \frac{1}{2}\left[1 - tanh(10(r_{OH} - 2.55))\right] \tag{4.4}$$

and

$$N = \frac{1}{2}\left[1 + cos(\pi(r_{OH} - 2.3)/(2.8 - 2.3))\right]. \tag{4.5}$$

The functions approach one at 2.3 Å and zero at 2.8 Å. TIP4P and TIP4P-FQ models with intermolecular charge transfer (referred to as CT-TIP4P and CT-TIP4P-FQ in this chapter), use equation 4.5, while equation 4.4 was used for the CT-FLEX model.

The total amount of charge is δq=(0.02 e)N. The contribution to the interaction energy is calculated in a fashion consistent with the DCT model by

$$E_{CT} = \mu_{CT}(N\delta q_t) + \frac{1}{2}\eta_{CT}(N\delta q_t)^2\,, \tag{4.6}$$

where μ_{CT} and η_{CT} are the chemical potential and hardness values, 10.67 kcal/mol/e and 308.11 kcal/mol/e^2, taken from *ab initio* calculations.[67]

The CT-TIP4P and CT-TIP4P-FQ models redistribute charges among the different atoms by the DCT method outlined in Chapter 3.[7, 24] The CT-FLEX model, however, does not have an automatic mechanism to redistribute charge. The CT-FLEX models charge distribution depends upon geometry and the number of hydrogen bond donors and acceptors, so the following matrix was chosen to determine the distribution.

$$\begin{pmatrix} q_O \\ q_{H_1} \\ q_{H_2} \end{pmatrix} = \begin{pmatrix} q_O^0 \\ q_{H_1}^0 \\ q_{H_2}^0 \end{pmatrix} + \begin{pmatrix} -0.0182 & -0.0182 & 0.016 \\ 0.0098 & -0.0116 & 0.002 \\ -0.0116 & 0.0098 & 0.002 \end{pmatrix} \begin{pmatrix} N_{H_1} \\ N_{H_2} \\ N_O \end{pmatrix} \tag{4.7}$$

The charge matrix 4.7 values were chosen so that the final charge distribution is the same as *ab initio* calculations, including dimerization geometry contributions. The values with the "0" notation refer to the initial charge values acquired by Equation 4.2. The matrix values are slightly different from those of the DCT model, varying mostly in the values for N_O. Each time a water molecule accepts a hydrogen bond, the bond angle of the accepting water molecule becomes larger. This increases the dipole. Simultaneously, the dipole of the donating water molecule reduces, due to the stretch in its O–H bond. The charge distribution of the water dimer then becomes consistent with electronic structure predictions.[72]

4.1.2 Simulation Details

Two types of simulations were carried out. The first was a system of 442 water molecules in a cubic box using periodic boundaries conditions. Equilibration time was 100 ps at a temperature of 298 K. The TPN ensemble was used and a Berendsen thermostat maintained the pressure and temperature.[61] The FLEX model was equilibrated for 1 ns to obtain equilibrium properties for comparison with experiment. The diffusion coefficient of water was calculated by equilibrating for 2 ns.

A tetragonal box was used to simulate the second type of system. The x and y directions were equivalent, with the z-axis elongated to 3–4 times the x and y dimensions. The TIP4P and TIP4P-FQ classes of models were systems of 1536 water molecules in a simulation box of 30 x 30 x 150 $Å^3$. The liquid occupies roughly 50 Å in the central portion of the box. The FLEX models were set up with 1000 water molecules in a simulation box, where the liquid populated about 24 x 24 x 40 $Å^3$ with a box z-dimension of 80 Å.

As mentioned previously, the FLEX model requires a smaller timestep of 0.2 fs, as compared to the 1 fs timestep of the TIP4P-type models. This allows the sampling of the faster vibrational degrees of freedom. SHAKE[171, 172] was used to constrain the rigid TIP4P-type models. The Lennard-Jones and Buckingham potentials were cut off at 12 Å with analytical tail corrections. TIP4P and TIP4P-FQ models implemented the regular Ewald summation. For the TIP4P and TIP4P-FQ simulations, the Lennard-Jones and real-space Ewald interactions were smoothly switched off from 12.0 to 12.5 Å.[3] The particle-mesh Ewald (PME) summation technique was used for the FLEX models.[173]

4.1.3 Results and Discussion

Bulk Properties for the CT-FLEX Model

Wick's CT-FLEX model, which incorporates the DCT method, was created specifically for this interface study. Bulk water simulations were carried out first to compare with experimental values, in order to determine the effects of charge transfer on the model's bulk properties. The results of these simulations are listed in Table 4.1. In this table, ρ is the liquid density, μ is the diffusion constant, and ϵ is the dielectric constant. Wick also calculated

Table 4.1: Comparison of the Properties of Pure Water Between Simulation Results for the CT-FLEX Model and Experiment at 298 K.

Property	CT-FLEX	Experiment
ρ_{liquid} (g/cm^3)	0.993 ± 0.001	0.995[174]
μ (m^2/s)	2.6± 0.2	2.3[175]
ϵ	80±6	78.3[176]

the radial distribution functions for his CT-FLEX model. He showed the charge transfer FLEX model is in very good agreement with his non-charge-transfer FLEX model and experiment, for which the O–H, O–O, and H–H radial distribution functions are published in Reference [166].

Density Profiles and Surface Tensions for the Liquid/Vapor Interface

The density profiles for all systems under study are given in Figure 4.1. The Gibbs dividing surface (GDS) was calculated using a hyperbolic tangent function.[110] The polarizable models show a slight increase in interfacial width with CT included. The TIP4P

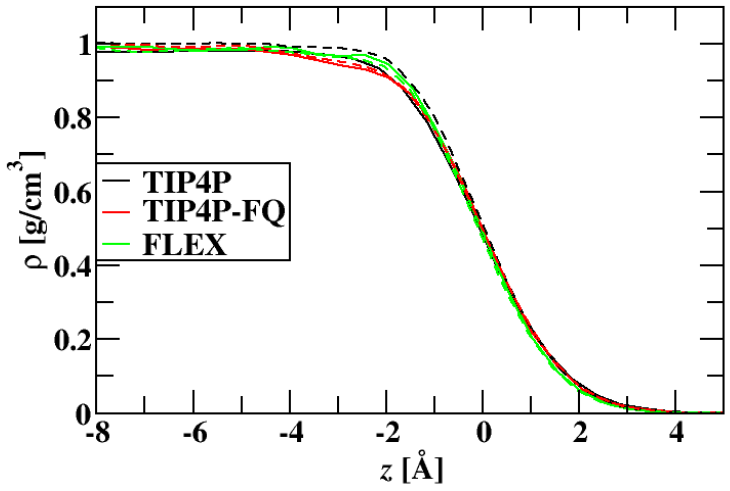

Figure 4.1: Average water density profile across the air/water interface as a function of z for the different water models investigated. Dashed lines have intermolecular charge transfer. Solid lines do not. The Gibbs dividing surface is at 0 Å.

model, however, shows a slight decrease. Pressure tensors were used to calculate the surface tensions by

$$\gamma = \frac{L_x}{2}\left[\frac{p_{xx}+p_{yy}}{2} - p_{zz}\right], \tag{4.8}$$

where γ is the surface tension, L_x is the box length, and the p variables are the values of the pressure tensor. The calculated surface tensions and interfacial widths are listed in Table 4.2. The experimental value for the surface tension of water is 72 dyn/cm.[177] The FLEX and CT-TIP4P models underestimate the surface tension. The TIP4P-FQ models,

however, do well in reproducing the experimental value. The original TIP4P model was

Table 4.2: Interfacial Widths and Surface Tensions for the Models Investigated

Model	Width (Å)	Surface Tension (dyn/cm)
TIP4P	3.19	50.9 ± 0.9
TIP4P-FQ	3.23	75.0 ± 1.0
FLEX	2.94	64.3 ± 1.5
CT-TIP4P	3.00	64.1 ± 1.2
CT-TIP4P-FQ	3.38	72.7 ± 1.0
CT-FLEX	3.00	64.9 ± 1.0

parameterized without accounting for the effects of long-range electrostatics and is notorious for underestimating the surface tension of water. TIP4P water also has a lower specific density than experiment; this may account for an incorrect surface tension value. Other studies show that rigid, non-polarizable water models underestimate the surface tension, with values around 50 to 60 dyn/cm, while rigid, polarizable models have surface tensions around 70 dyn/cm.[178] That the polarizable FLEX model has a smaller surface tension than other polarizable models may indicate that flexibility decreases the surface tension. Charge transfer does not seem to have a significant effect on the surface tension.

Interfacial Dipole and Surface Relaxation

Air and water are dramatically different dielectrics. The electronic structure of polarizable models, therefore, changes at the interface, responding to the dielectric difference. The combination of intermolecular interactions resulting from charge rearrangement and charge transfer due to asymmetry in the HB structure at the air/water interface leads to a significant decrease in the dipole moment at the surface versus the bulk value. Figure 4.2 compares the interfacial dipole moments of all models in this study. By construction, the dipole moment of the non-polarizable TIP4P model remains constant. Figure 4.2 shows that the inclusion of charge transfer lowers the dipole moment of all the models in the bulk. We

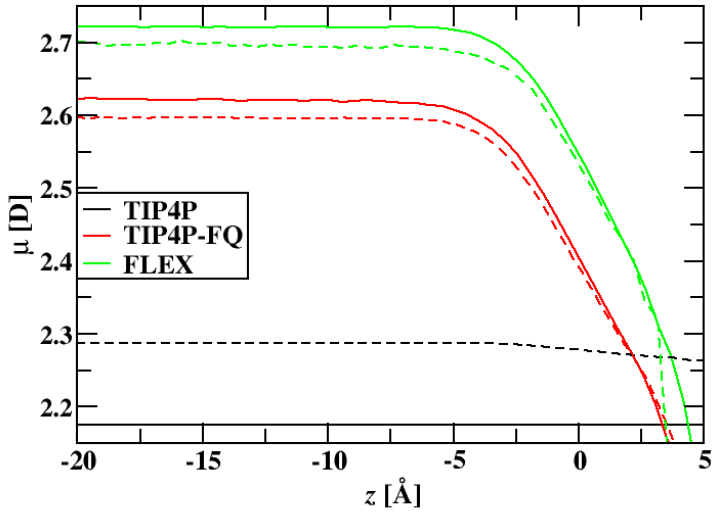

Figure 4.2: Profile of the average total dipole of water across the air-water interface for the different water models investigated. Dashed lines have intermolecular charge transfer.

surmise this effect could be due to the lowering of electrostatic interactions to compensate for the CT addition to the energy.

The polarizable models show expansion at the surface, due to a lower dipole moment that cause weaker intermolecular cohesive energies. Interfacial expansion has been documented experimentally.[163] The average surface O–O distances minus the average bulk values for each model are plotted as a function of z-position in Figure 4.3, characterizing the first solvation shell of the interfacial water molecules. In this study, the first solvation shell has been defined as two oxygens with a separation of 3.3 Å or less. This definition corresponds to the first peak seen in the oxygen-oxygen radial distribution function. The observed surface expansion with the CT-TIP4P-FQ model is a feature of the TIP4P-FQ model. Consistent with previous studies, the non-polarizable models show a slight surface contraction.[141, 142]

Molecular Charge Density Across the Air/Water Interface

The total charge on each molecule depends on the number of hydrogen bonds a molecule makes as a donor and as an acceptor, as per the DCT model. High HB asymmetry at the surface means more molecules will have an unequal number of donor and acceptor

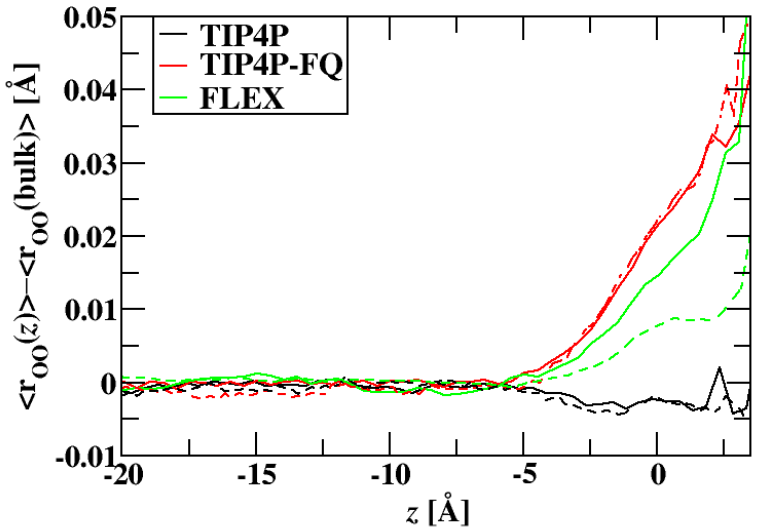

Figure 4.3: Profile of the average distance between first solvation shell water oxygens minus the average bulk distance across the air-water interface for the water models investigated. Dashed lines have intermolecular charge transfer.

bonds, giving a molecule a nonzero charge. The position of the hydrogens on a molecule near the interface will dictate whether that molecule donates more or less hydrogen bonds. If one or both hydrogens are pointing out of the bulk water, the molecule will accept more hydrogen bonds than it donates, due to the lone pair pointing into the bulk. This will give a positive molecular charge. The converse is also true, in accordance with the DCT method. Plotted in Figure 4.4 is the hydrogen bond distribution, the averaged difference between number of acceptor and donor bonds a molecule makes as a function of z. Figure 4.4 illuminates the different charge layers near the interface of water and air. At 1 Å and greater, toward the vapor-side of the GDS, a population of positively-charged water molecules is seen. This means more hydrogen bonds are being made as an acceptor versus donor hydrogen bonds per water molecule. Moving along the z-coordinate toward the bulk water, a negative trend occurs, signifying a negatively-charged layer of water molecules to about 3 Å into the bulk. A third, slightly positive layer can be identified between 3 and 8 Å. From z = 8 Å into the bulk water, $n_{acceptor} - n_{donor}$ averages to 0.

The molecular charge density and integrated charge as a function of z are depicted in Figures 4.5 and 4.6, respectively, for the polarizable charge transfer models. All the

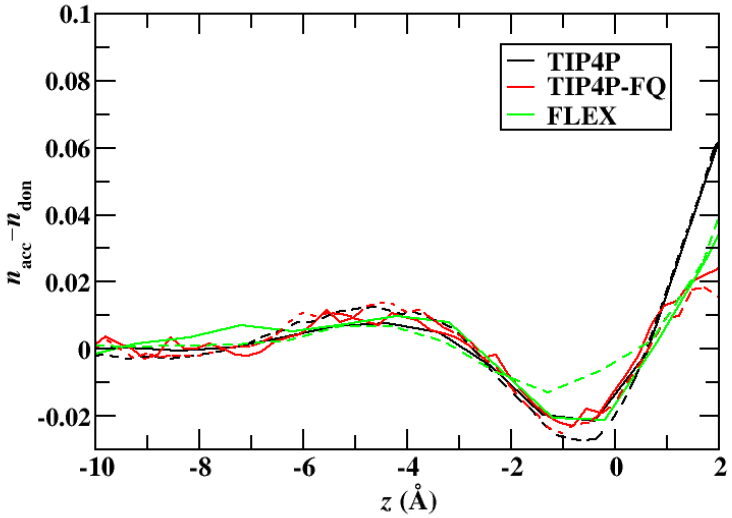

Figure 4.4: Difference in number of hydrogen bond acceptors and donors as a function of z for the water models investigated. Dashed lines represent the intermolecular charge transfer models.

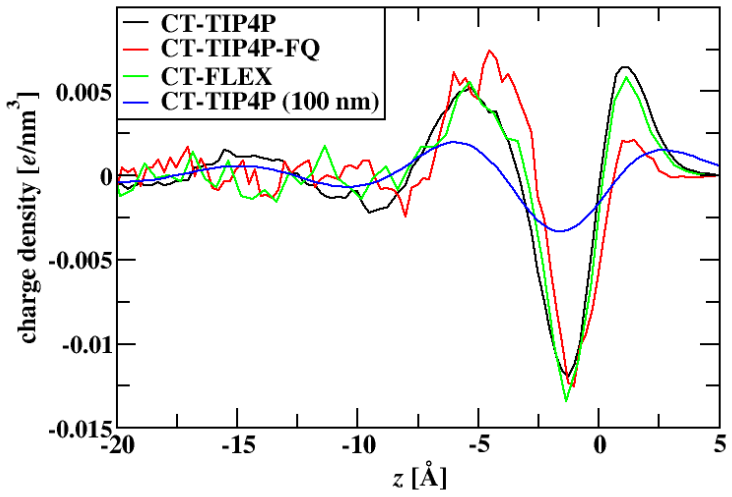

Figure 4.5: Molecular charge density profile as a function of z for the charge transfer models, with an estimate of the charge distribution for the CT-TIP4P water model with an interfacial cross section of 100 nm.

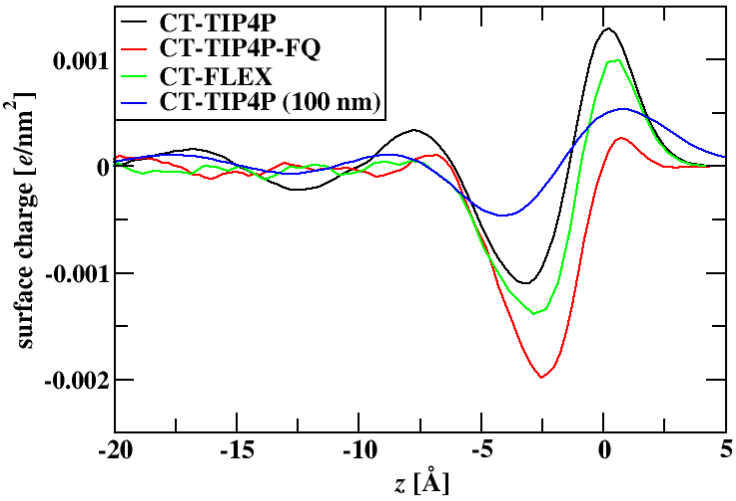

Figure 4.6: Integrated charge as a function of z for the charge transfer models, with the integrated estimate of the charge distribution for the CT-TIP4P water model with an interfacial cross section of 100 nm.

charge transfer models exhibit similar qualitative behavior, with an aggregation of positively-charged molecules at the surface, followed by a compensating negative layer. The charges then disperse and average to neutrality into the bulk. The positive region is indicative of dangling hydrogens, or non-hydrogen-bonded surface water hydrogens. It has been theorized that the compensating negatively-charged layer is responsible for experimental evidence showing a negative surface charge for water.[143] These surface calculations are consistent with predicted values for the hydrophobic water/decane interface carried out by mapping hydrogen bonds at the surface and calculating predictions.[55] The fluctuating charge TIP4P models show, as all the models studied, a greater number of acceptor bonds at 2 Å. This difference, however, is smallest for the TIP4P-FQ models, corresponding to the smallest positive charge region at that z-coordinate in Figures 4.5 and 4.6. This is at a low average density region of the interface, so this corresponds to a relatively small number of molecules. The inclusion of intermolecular charge transfer appears to be negligible for the TIP4P-FQ models. Charge transfer may increase the number of donors for TIP4P, but the number is reduced for the FLEX model.

Electrostatic Potential Across the Air/Water Interface

Electrostatic potential as a function of z across the air/water interface was calculated for all 6 models using the atomic approach (See References [159, 160, 161]) and plotted in Figure 4.7. The potential difference between the two phases, liquid and vapor, is of

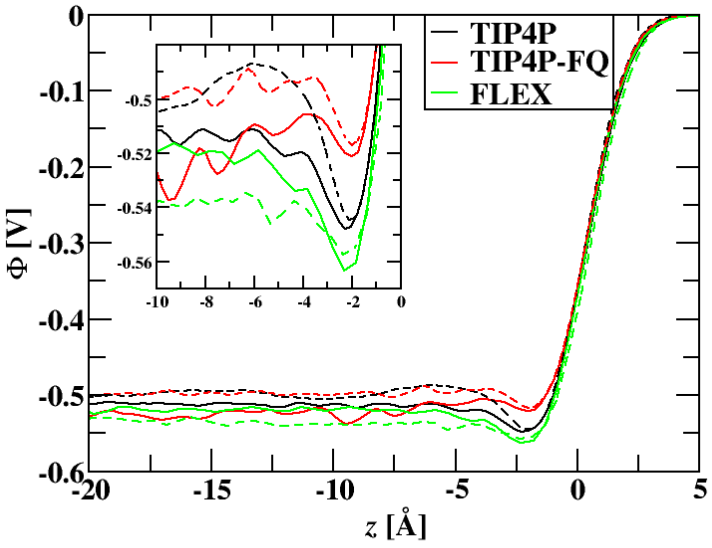

Figure 4.7: Electrostatic potential as a function of z across the air/water interface. Dashed lines are charge transfer models. The inset is an enhanced view near the GDS.

particular interest, and the two extremes are to be compared. Consistent with many other water potential models, the models in this study gave surface potential values between -0.5 and -0.564 V. The models without charge transfer yielded surface potentials that were lower than those with charge transfer included. Adding charge transfer decreases the surface potential for the CT-TIP4P and CT-TIP4P-FQ models. Inclusion of charge transfer to the 6 potentials had little effect on the surface potentials for each model.

4.1.4 Conclusion

The inclusion of charge transfer in simple potential models has been determined to be, for the most part, ineffective for the neat water/air interface. Polarizable charge transfer models have the greatest influence on interfacial expansion and interfacial charge distribution. This study has shown charge transfer models causes a slight positive charge at the

interface of air and neat water, followed by a compensating negatively-charged layer, a subsequent partial-positive layer, averaging to neutrality into the bulk. The charge separation is dependent upon the model used.

4.2 Charge Transfer at the Ice/Liquid Water Interface

4.2.1 Introduction

Water frozen under ambient pressure forms hexagonal crystals with an oxygen positioned at each vertex. This form of ice is known as ice I_h and is the most common water ice structure found in nature. The subscript h denotes the "hexagonal"[179, 180, 181, 182], setting apart this ubiquitous, stable structure from the metastable *c*ubic form, ice I_c, which is theorized to exist naturally the tropical tropopause layer (TTL) of the Earth's atmosphere, where temperatures range between 120–200 K.[183, 184, 185]

Although the oxygens of ice I_h construct an ordered sub-lattice, the hydrogen arrangement is disordered, meaning aperiodic, or devoid of a regular and repeating pattern in the lattice cell. The water molecules of ice I_h must satisfy the bonding stipulations postulated by Bernal and Fowler (1933), known as the "ice rules". The ice rules state that each oxygen is covalently bonded to 2 hydrogen atoms, i.e., its own hydrogens, and hydrogen bonded to 2 other waters, so that exactly 1 hydrogen is situated between each O–O pair. These bonding requirements are satisfied by a near-tetrahedral geometry.[131, 132, 182, 186, 187, 188]

Ice I_h may be obtained simply by crystallizing liquid water at ambient conditions or by direct condensation from water vapor at supercooled temperatures, as in cirrus and altostratus/altocumulus clouds–the most prevalent cloud types in Earth's atmosphere, mainly comprised of ice particles.[189, 190]

It should be noted that several studies of water's freezing mechanism over the past few years have challenged the long-held belief that hexagonal ice is the dominant nucleating species over cubic ice. Ostwald's rule of stages [191] predicts the metastable state [of ice] will nucleate before the thermodynamically-stable state is attained, e.g, cubic ice nucleates and crystalizes first. Murray and Bertram explain that a thermodynamically-favorable transition from ice I_c to ice I_h then occurs, due to the higher chemical potential of ice I_c.[183, 184, 185] The phase diagram of water reveals a myriad of structures for ice, including metastable

and amorphous phases, a new "stacking disordered" phase (ice I_{sd}), a combination of layers of stacked ice I_h and I_c, and new phases occurring at very high pressures.[192] This text, however, focuses on proton disordered hexagonal ice, ice I_h, and will henceforth be referred to simply as "ice".

The bonding situation for ice in the bulk, where there is very high hydrogen bond (HB) symmetry, has been well established.[186, 187] Experimental and theoretical techniques characterizing the surface of ice, where HB symmetry is broken, indicate the ice surface is constructed of 3 types of water molecules:

1. water with dangling O–H bonds,
2. water with dangling unoccupied bonds,
3. four-co-coordinated water molecules in a distorted tetrahedral geometry.[193, 194]

The asymmetry of the local bonding environment of the ice surface lends itself to charge transfer interactions.

The method of Discrete Charge Transfer (DCT) proposed by Lee and Rick (2011)[24] has been implemented to investigate effects of charge transfer at ice/liquid water interface. The high symmetry of the bulk water molecules provides no driving force for charge transfer.[12] The asymmetrical local environment of the ice/liquid water interface is predicted to give rise to significant surface charge transfer effects. Considering the rise in CT phenomena at the liquid water/vapor interface due fluctuating hydrogen bonds, we expect the ice/liquid water interface to be particularly interesting.

4.2.2 Methods

The polarizable potential, TIP4P-FQ+DCT was applied to a system of 1440 ice and liquid water molecules in a 22.6 x 23.1 x 84.85 $Å^3$ box. Temperature was maintained at 200 K using a Nosé-Hoover thermostat. The Discrete Charge Transfer (DCT) method dictates that charge transfer per hydrogen bond is a fixed number, suited to the system under study.

The CT value used in this study is -0.02 e, consistent with previous studies of pure water systems. An O$\cdots$H distance between neighboring water molecules in the range of 0 and 2.8 Å was considered a hydrogen bond. A switching function was implemented from 2.3 Å to 2.8 Å to smoothly turn off interaction. The temperature was held at 200 K, well below the published melting temperature of 302 K (See Table 4.3), because a stable interface at higher temperatures could not be established. Simulation time of the results presented is 1.2 ns. For in-depth simulation details, the reader is referred to Lee and Rick (2011)[24], the DCT

Table 4.3: Temperature of the ice/water charge transfer simulation and the melting temperature for the model found by Chung and Rick[12].

Model	T (K)	T_M (K)
TIP4P-FQ+DCT	200	302

method.

4.2.3 Results and Discussion

A stable yet fluctuating ice/water interface was established at 200 K. The molecular density profile in Figure 4.8 shows a highly-structured ice region from approximately -5 to -42 Å. A semi-crystalline layer is positioned between -5 and +5 Å. This "quasi–liquid layer"[182] is three times the size of the the published width for the ice/vapor interface (3.2 Å at 298 K).[110] As the simulations progress, the dimensions of this region are expected to fluctuate. The liquid layer is relatively stable and about 20 Å in width, with an average density near 1 g/cm^3.

Figure 4.9 is a plot of the dipole moment as a function of z. The ice I_h dipole moment is approximately 2.9 Debye, close to the value reported by Batista, Xantheas, and Jónsson (3.1 Debye)[195], computed employing first principles methods. A range of dipole moments, from 2.3 to 3.1 Debye, was reported for their ice I_h systems, depending on the partitioning scheme used. Before that study, Silvestrelli and Parinello calculated the liquid dipole moment to be 3 Debye.[196] The dipole moment of the liquid phase is 2.6 Debye, which is consistent

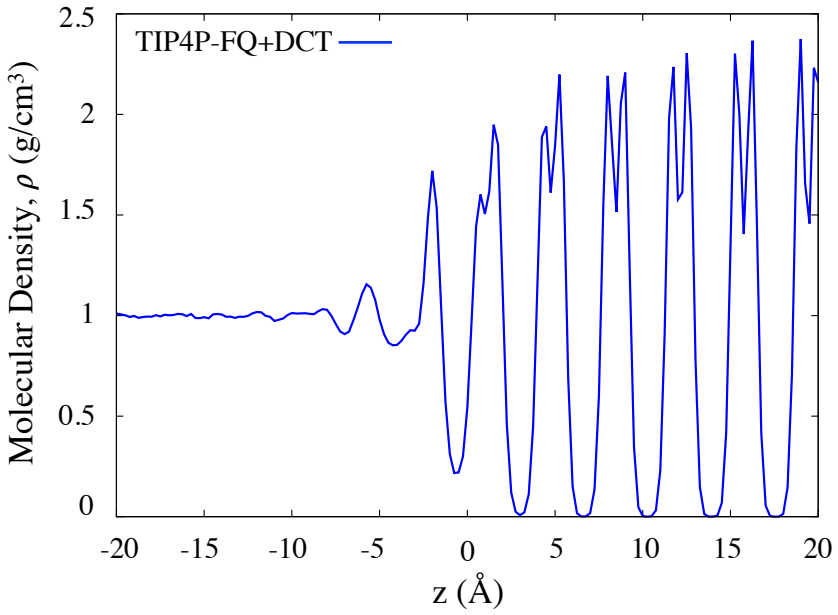

Figure 4.8: Molecular density profile for the ice/liquid interface with TIP4P-FQ+DCT water as a function of z.

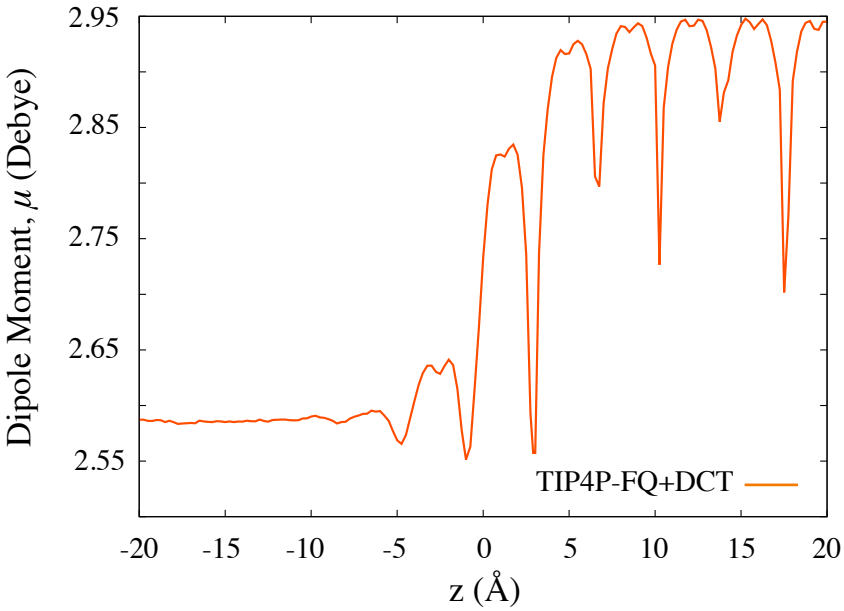

Figure 4.9: Dipole moment of the ice/liquid interface with TIP4P-FQ+DCT water as a function of z.

with the established value for the TIP4P-FQ+DCT model, 2.596 Debye at 298 K.[12] The interfacial dipole moment decreases steadily from -5 and +5 Å, with an average value of 2.75 Debye at z=0 Å. The liquid- and ice-phase dipole moments obtained by this study are lower than those given by bulk ice TIP4P-FQ (2.641±1 Debye for the liquid; 3.097±1 Debye for ice I_h). The dipole moment determined by this study is only slightly under the Chung and Rick value for TIP4P-FQ+DCT. This could be due to a difference in polarization parameters. [4] Charge transfer seems to decrease the dipole moment of the two phases.

Figure 4.10 is the charge density profile as a function of the z-coordinate. As expected, an unequal number of hydrogen bond donors and acceptors are located near the interface. The region of interest between -5 and +5 Å shows a similar trend to that of the liquid/vapor interface, but more pronounced, with more layers of partial positive and partial negative charge. As the z-coordinate progresses into the bulk phases, the charges disperse and average to 0 e. In Figure 4.8, negative z values correspond to the liquid phase and positive to the ice phase.

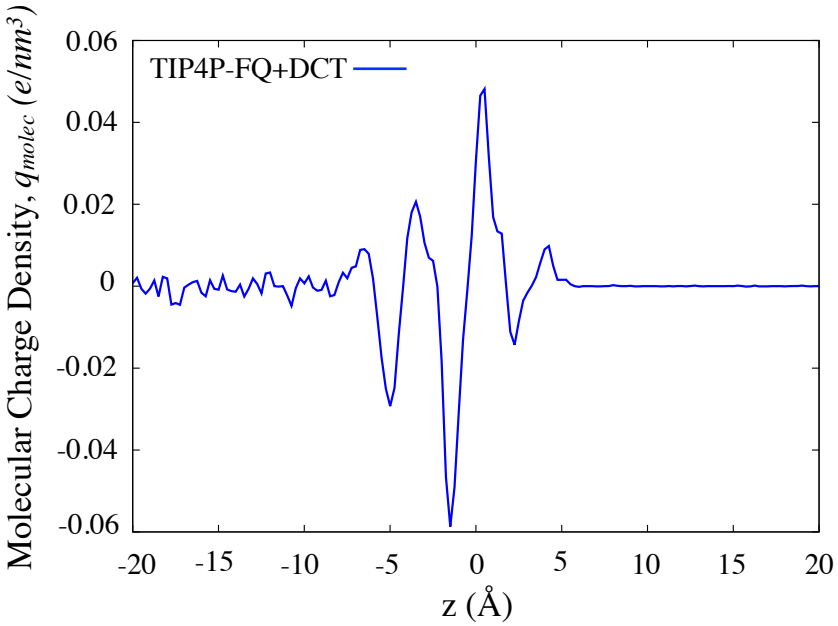

Figure 4.10: Molecular charge density profile at the ice/liquid interface with TIP4P-FQ+DCT water as a function of z.

Integrating the charge density gives the surface charge, q (e/nm^2). Figure 4.11 illustrates the surface charge due to asymmetry in hydrogen bonds at the ice/liquid interface. Increased charge in the semi-crystalline layer between -5 and +5 Å is a result of charge transfer, as dictated by DCT.

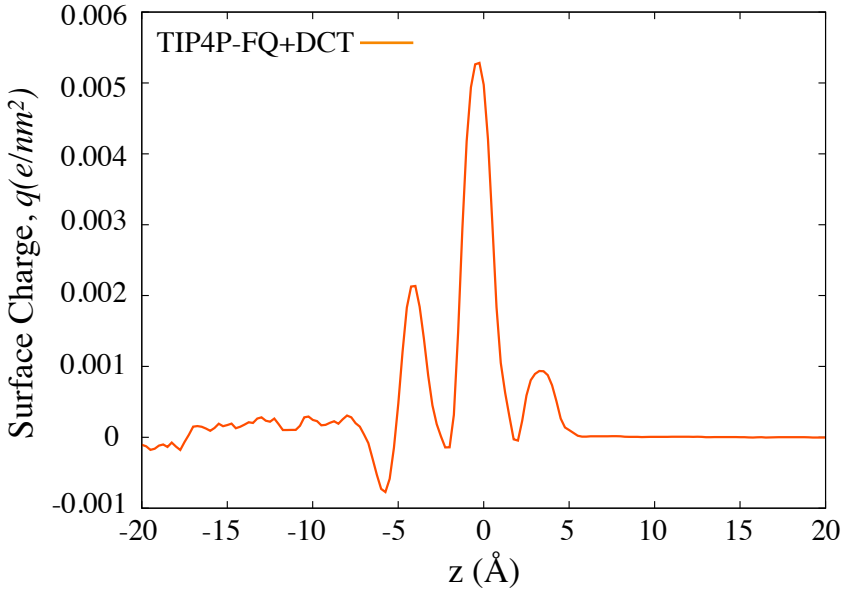

Figure 4.11: Surface charge at the ice/liquid interface with TIP4P-FQ+DCT water as a function of z.

The surface charge data indicate the number of hydrogen bond acceptors, $n_{acceptors}$, is greater near the interface than n_{donors}. An interesting feature of Figure 4.11 is the increased surface charge (about 0.0055 e/nm^2) compared to the largest peak of the liquid/vapor surface charge, -0.002 e/nm^2. The integration over surface charge begins in the ice region, so that a positive integrated surface charge indicates a net positive charge at the ice side of the interface. There is a net negative charge at the liquid side of the interface

4.2.4 Conclusion

The interfacial charge distribution of the ice/liquid water interface exhibits more effects from charge transfer than that of the liquid/vapor interface both in charge magnitude and charge composition of the local environment near the interface. A greater population

of hydrogen-bond acceptors is located near the ice/liquid interface than at the liquid/vapor interface, making the ice/liquid interface more positively charged. The peaks of the molecular charge are 0.06 e/nm^3 for the ice/water interface and about 0.01 e/nm^3 for the liquid/vapor. Similarly, for the integrated charge, the ice/liquid system has a peak over 0.005 e/nm^2, whereas the liquid/vapor surface peak is around 0.002 e/nm^2. An unexpected result is the magnitude of the charge of each oppositely-charged layer of the interface, which is about five times bigger than layer charges for the liquid/vapor surface (See Figure 4.6). It seems counterintuitive that more positive charge would exist at the ice/water interface than at the liquid/vapor interface because the waters of the L/V surface have more room for dangling O–H bonds and dangling unoccupied bonds. Perhaps the rigidity of the ice lattice lends itself to more HB donation than water interacting with itself, as in the liquid/vapor interfacial region. Capillary waves in the liquid may be the cause of decreased surface charge for the liquid phase. Future work on this matter will be similar to the study concerning the liquid/vapor interface, in that the ice/vapor interface will be investigated and non-polarizable and non-charge-transfer potentials utilized.

Chapter 5

Improving Replica Exchange using Driven Scaling

5.1 Introduction

Many interesting molecular systems have important regions of conformational space separated by large energy barriers, which presents a challenge for molecular dynamics and Monte Carlo simulations. One general method to overcome the ergodicity problem is replica exchange (See Reference [197] and references therein). In replica exchange (RE), a number of simulations of the system are run in parallel, so that the system with sampling problems (presumably under the conditions of interest) is linked to a system which can easily overcome energy barriers (with an elevated temperature or a modified potential surface). Swaps between the different replicas are accepted with a probability that gives the correct Boltzmann weighting. In order for exchanges to be accepted, there has to be some overlap in the energy distributions of the replicas. This establishes how far apart in temperature the replicas can be and as the number of degrees of freedom, f_s, of the system increases, the number of replicas required to span the same temperature increases as approximately $f_s^{1/2}$.[198] The poor scaling of the method places practical limits on the system sizes that can be studied with replica exchange. One of the largest studies is the folding of a 12 amino acid polypeptide with 3604 water molecules, which required 80 replicas to span a temperature

This chapter has been published previously as a paper in the Journal of Chemical Physics, *131*, 174113 (2009): "*Improving replica exchange using driven scaling*".

range of 245 to 600 K, an average spacing between replicas less than 5 K.[199] Other studies of similarly-sized polypeptides require large number of replicas.[200, 201, 202]

Replica exchange studies of larger systems, including small proteins, will require more efficient methods. A number of methods have been developed to reduce the number of replicas, which can involve quenching or annealing[203, 204, 205, 206, 207], the multicanonical algorithm (MUCA)[208, 209, 210], simulated tempering (ST)[211, 212], and Hamiltonian RE.[198, 211, 213, 214, 215, 216, 217] A method developed in our group, Replica Exchange with Dynamical Scaling (REDS), shows promise as a general method for gaining efficiency.[218] The REDS method places between two distant replicas at temperatures T_A and T_B, a replica at an intermediate temperature, T_M, with an energy given by

$$E_\lambda(r) = \left[\frac{T_M}{T_A}\lambda + \frac{T_M}{T_B}(1-\lambda)\right] E(r), \tag{5.1}$$

where E(r) is the potential energy of the system. The variable λ is constrained in the interval from 0 to 1. If $\lambda = 0$, then the Boltzmann weighting of the system is exp[-(T_M/T_B)E(r)/$k_B T_M$]=exp[-E(r)/$k_B T_B$], or the same as that at the temperature, T_B (where k_B is Boltzmann's constant). Because the configuration would have the same Boltzmann weighting for both replica B and the intermediate replica, an exchange between the two replicas would be accepted with probability 1. The same would be true with replica A when $\lambda = 1$. In this way, as λ varies from 0 to 1, the replica can exchange with both neighboring replicas, even if they have temperatures that are widely separated. The variable λ is made to vary by treating it as a dynamical variable, with a mass and equations of motion, as is done in other λ-dynamics applications.[219, 220, 221, 222, 223, 224, 225, 226] In the first application of this method to the alanine dipeptide with 512 water molecules, the scaled replica was shown to replace about 10 conventional replicas, reducing the number of replicas from 22 to 5. The method has some other advantages. Unlike other Hamiltonian RE methods, the modified replicas can give correct ensemble averages, for the entire range of temperature

from T_A to T_B. The method can also be used in the isothermal-isobaric ensemble by scaling E+PV, where P is pressure and V is volume, rather than just E in Equation 5.1.

One disadvantage of REDS over conventional RE is that in order to ensure that λ varies evenly between 0 to 1, a biasing potential must be used. The biasing potential would have to be determined prior to the simulation, increasing the setup time. Conventional RE also has setup time involved in the determination of the optimal set of temperatures to use.[227, 228, 229, 230] The other RE methods MUCA[208, 209, 210], ST[211, 212], and quenching/anealing methods[204, 205, 207] also require a biasing (or weight) factor, to ensure proper Boltzmann weighting. For the REDS method, the biasing potential can be constructed only from an estimate of the potential energy over the temperature range, T_A to T_B. In practice, a good biasing potential can be constructed from values of the potential energy at T_A, T_B, and T_M. Finding the potential energy is typically much easier than calculating the MUCA weights, which require the entropy over an energy range, or the ST weights, which require the Helmholtz free energy at different temperatures. The potential energy is particularly easy to estimate if the system's degrees of freedom are mostly water molecules, so the energy is dominated by the contributions from the water-water interactions, which can be calculated without advanced sampling techniques.

A variation of the REDS method in which λ, rather than being a dynamical variable, is given an explicit time dependence and made to cycle from 0 to 1 and back again over some time scale, τ, is presented. This eliminates the need to determine the biasing potential and only requires choosing τ. The system is now driven externally as λ changes. This chapter presents the new method, REDS2, and its application to two different systems, the alanine dipeptide with 512 water molecules, and a 12-amino-acid peptide which has a stable fold (the trpzip2 peptide[231]) with 2434 water molecules.

5.2 Methods

In the replica exchange with driven scaling (REDS2) method, some replicas have a time-dependent energy function (Equation 5.1) and others have the standard potential energy, E(r). The parameter λ is given an explicit time dependence,

$$\lambda = \sin^2(\pi t/\tau), \tag{5.2}$$

so that λ ranges from 0 to 1 over a time scale τ. Exchanges between the configurations, r_M, of a driven replica at a temperature, T_M, and the configurations, r_N, of a normal replica at a temperature, T_N, with T_N corresponding to either T_A or T_B in Equation 5.1, are accepted so that they satisfy detailed balance. Detailed balance is given by

$$\rho(r_N, T_N)\rho(r_M, T_M)T(N \to M) = \rho(r_N, T_M)\rho(r_M, T_N)T(M \to N)\,, \tag{5.3}$$

where T(N$\to$ M) is the transition probability for the exchange between N and M. The densities are given by

$$\rho(r_M, T_M) = e^{-(\lambda T_M/T_A + (1-\lambda)T_M/T_A)E(r_M)/k_B T_M}/Z_M = e^{-(\lambda/T_A + (1-\lambda)1/T_A)E(r_M)/k_B}/Z_M\,, \tag{5.4}$$

for the driven replica, and

$$\rho(r_N, T_N) = e^{-E(r_N)/k_B T_N}/Z_N\,, \tag{5.5}$$

for the standard replica, with Z_j being the configurational partition function. Equation 5.4 is the major assumption of the REDS2 method. It assumes that the configurations are in equilibrium with the time-dependent Hamiltonian and do not show any hysteresis. This will be true in the limit that τ goes to infinity and would have to be verified for finite values.

Using Equations 5.4 and 5.5, detailed balance is then

$$e^{-(\lambda/T_A+(1-\lambda)/T_A)E(r_M)/k_B}e^{-E(r_N)/k_BT_N}/(Z_MZ_N)T(N\rightarrow M) =$$

$$e^{-(\lambda/T_A+(1-\lambda)/T_A)E(r_N)/k_B}e^{-E(r_M)/k_BT_N}/(Z_MZ_N)T(M\rightarrow N). \tag{5.6}$$

The ratio of the transition probabilities is

$$T(N\rightarrow M)/T(M\rightarrow N) = e^{\Delta_{NM}}\,, \tag{5.7}$$

where

$$\Delta_{NM} = \left[\frac{\lambda(t)}{k_BT_A} + \frac{1-\lambda(t)}{k_BT_B} - \frac{1}{k_BT_N}\right][E(r_M) - E(r_N)]\,, \tag{5.8}$$

which can be satisfied with the Metropolis criteria[232],

$$P(N\leftrightarrow M) = \min(1, \mathrm{e}^{\Delta_{\mathrm{NM}}}). \tag{5.9}$$

P(N$\leftrightarrow$M) gives the probability of switching the coordinates of replica M, r_M, with the coordinates of replica N, r_N. Equations 5.8 and 5.9 represent a special case of the acceptance criteria for Hamiltonian RE.[198] Because the modification of the Hamiltonian is simple, the resulting value for Δ_{NM} is close to that for conventional RE, in which $\Delta_{NM} = (1/k_BT_M - 1/k_BT_M)[E(r_M) - E(r_N)]$. From Equation 5.8, it is evident that exchanges will be accepted automatically when λ(t)=1, with the replica at T_N=T_A, and when λ(t)=0, with the replica at T_N=T_B.

The driven replica can not only bridge between two replicas far apart in energy, but it can also, like the REDS method, generate ensemble averages over the temperature range from T_A to T_B.[218] The canonical ensemble average of a property A at a temperature T_i is

$$\langle A\rangle_{T_i} = \frac{\int dr\; A(r)\; e^{-E(r)/k_BT_i}}{\int dr\; e^{-E(r)/k_BT_i}} = \frac{\int dr\; d\lambda A(r)\; \delta(\lambda-\lambda_i)\; e^{-E(r)/k_BT_\lambda}}{\int dr\; d\lambda\; \delta(\lambda-\lambda_i)\; e^{-E(r)/k_BT_\lambda}}, \tag{5.10}$$

where

$$T_\lambda = (\lambda/T_A + (1-\lambda)/T_B)^{-1}, \tag{5.11}$$

and, with T_{λ_i}=T_i,

$$\lambda_i = (1/T_i - 1/T_B)/(1/T_A - 1/T_B). \tag{5.12}$$

The denominator on the left side of Equation 5.10 is related to the probability distribution of λ,

$$\langle P(\lambda_i)\rangle = \int dr\, d\lambda\, \delta(\lambda - \lambda_i)\, e^{-E(r)/k_B T_\lambda}/Z_M\,, \tag{5.13}$$

and the numerator is related to

$$\langle A(\lambda_i)\rangle = \int dr\, d\lambda\, A(r)\, \delta(\lambda - \lambda_i)\, e^{-E(r)/k_B T_\lambda}/Z_M\,, \tag{5.14}$$

so that

$$\langle A\rangle_{T_i} = \langle A(\lambda_i)\rangle/\langle P(\lambda_i)\rangle\,. \tag{5.15}$$

Both $\langle A(\lambda_i)\rangle$ and $\langle P(\lambda_i)\rangle$ can be calculated from the driven replica. Equation 5.15 is valid only if Equation 5.4 is valid, that is, if the coordinates are in equilibrium with the time-dependent potential. It is worth emphasizing that the driven replicas remain at a constant temperature; only the potential is being scaled in a way that can give ensemble averages over a range of temperatures. The method does not involve varying the temperature over some range, as in simulated tempering, or using temperature quenches.

Simulation details. Two different systems were used. The first is the alanine dipeptide using the OPLS-AA/L potential[233, 234] with 512 TIP4P[6] water molecules. This was simulated using our out own program with a timestep of 1 fs, SHAKE[171, 172] to constrain all bonds, Ewald for long-ranged electrostatic interactions, and Nosé-Hoover chains for thermostatting. To examine how well the REDS2 method performs, we will compare the results using conventional RE with 22 replicas and REDS2 with 5 replicas, 3 conventional replicas (at T=300, 420, and 600 K) and 2 driven replicas (at T=350 and 494

K). These are the same temperatures used in a previous study with conventional RE and REDS[218] and were chosen according to the relation T_i=T_0exp(ic), as proposed by Sugita and Okamoto.[235] The REDS2 method used a time constant, τ, equal to 50 ps, except as noted. Simulations were run twice for each method, once with all replicas in a $C7_{eq}$/C5 configuration (ϕ=-60° and ψ=-150°) and once with all replicas in a $\alpha_R/\beta 2$ configuration (ϕ=-60° and ψ=0°). Each replica of the 22-replica system was simulated for 6 nanoseconds for a total simulation time, counting all the 22 replicas and both initial conditions, of 264 nanoseconds. Each replica for the 5 replica system with the REDS2 method was simulated for 16 nanoseconds, totaling 160 ns of simulation time.

The second system is the 12-amino-acid tryptophan zipper, trpzip2[231], peptide using the ff99SB[236, 237] force field (shown to accurately reproduce the trpzip2 structure for trpzip2[237]) with 2434 TIP3P[6] water molecules and one chloride ion for charge neutrality. The trpzip2 simulations were done by our own modifications to the Amber9 suite of programs.[238] These simulations used 1 fs time step, SHAKE, particle-mesh Ewald summations, and a Langevin heat bath to maintain a constant temperature. For the trpzip2 system, the REDS2 method was compared to the REDS method. Both methods used replicas to span a temperature range from 250 K to 600 K. This is similar to the temperature range of 250 K to 640 K used in a previous RE simulation, which had about the same system size (with 2433 water molecules) and required 62 replicas.[201] Our implementation of REDS2 used 10 replicas (5 scaled at 273, 320, 369, 436, and 533 K and 5 unscaled at 300, 343, 400, 480, and 600 K) and τ=200 ps (except as noted). The REDS method used 16 replicas (8 scaled at 261, 286, 313, 343, 379, 424, 450, and 514 K and 8 unscaled at 273, 300, 327, 360, 400, 450, 514, and 600 K). The REDS method used a mass for λ equal to 0.1 kcal/mol/ps. In addition, rather than enforcing the condition that λ stays in the interval from 0 to 1 by changing variables as done previously[218], we placed elastic hard walls at $-\epsilon$ and $1+\epsilon$, with ϵ=0.005 Å.[226] The scaled replicas have T_A and T_B values equal to the temperatures of the adjacent replicas; for the scaled replica with the lowest temperature, T_A equals 250 K. All

replicas for both methods started from an unfolded state, which was generated by starting with the folded structure of trpzip2[231], running at 640 K for 1.2 ns, and then equilibrating this unfolded structure at lower temperatures. The REDS results represent 10 ns per replica, and the REDS2 results represent 14 ns per replica.

5.3 Results and Discussion

In order to implement the REDS2 method, a value for τ must be chosen. It is important that τ, which determines the timescale for the Hamiltonian scaling, is not too short, so the coordinates of the system can stay in equilibrium. Proximity to equilibrium can be checked by monitoring properties of the system as a function of λ. Using Equation 5.15 properties of the driven replica can be related to the properties from standard simulations at the appropriate temperature. Energies are used to check equilibrium proximity, rather than structural properties, since the equilibrium structure is not always known and reaching equilibrium for structural properties can be slow. If we start simulations with coordinates equilibrated at λ equal to 0 and run until λ equals 1 (this will be a time equal to $\tau/2$), we can compare different values of τ. Figure 5.1 shows E_λ versus time for both the alanine dipeptide and trpzip2 systems, both with the same scaling parameters (T_A=300, T_B=420, and T_M=350 K). The systems are equilibrated with λ equal to 0, which gives coordinates equivalent to a temperature of 420 K and an energy equal to (350 K/420 K)$\langle \mathrm{E} \rangle_{420K}$, or the energy at 420 K times a scaling factor. As time goes to $\tau/2$, λ goes to 1 and the energy should approach (350 K/300 K) $\langle \mathrm{E} \rangle_{300K}$. The curves for the alanine dipeptide show τ equal to 1, 2, and 20 ps. With τ, the coordinates are in equilibrium with E_λ, and values greater than 20 ps are essentially the same. The curves for trpzip2 show τ equal to 5, 10, and 40 ps. For this system, the coordinates appear to be in equilibrium for τ greater than or equal to 40 ps.

The value of τ required to maintain equilibrium is system dependent, as shown in Figure 5.1. The trpzip2 system is greater by a factor of four or five than the alanine dipeptide

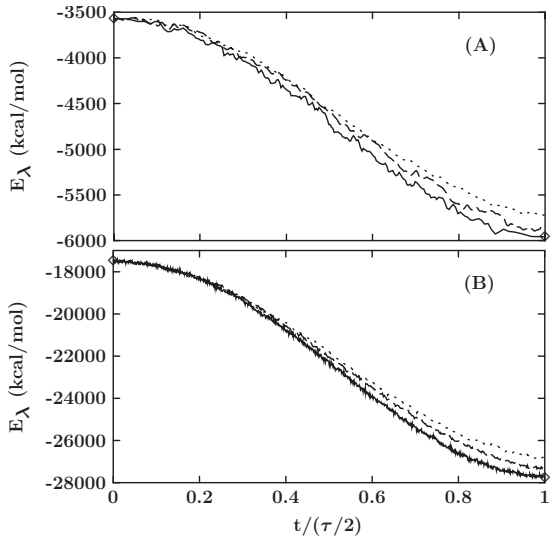

Figure 5.1: Scaled energy, Eλ versus time for (A) the alanine dipeptide system with τ= 1 (dotted line), 2 (dashed line), and 20 ps (solid line) and (B) the trpzip2 system with τ=5 (dotted line), 10 (dashed line), and 40 (solid line) ps. The diamonds show the equilibrium values for Eλ.

system, largely due to the difference in the number of water molecules (2434 compared to 512). The required τ increases by about a factor of two (20 ps to 40 ps), going from the alanine dipeptide to the trpzip2 system. This timescale is related to the energy fluctuations. The energy for both systems is dominated by water-water interactions because water molecules make up the large majority of degrees of freedom. The most significant factor for the energy difference is the number of water molecules, rather than the different solutes. Fluctuations in the energy, δE, are related to the heat capacity through $\delta E^2 = k_B T^2 C_V$, and so, because the heat capacity increases with the number of particles, N, δE increases only as $N^{1/2}$. Fluctuations as a fraction of the energy, which increases linearly with N, decrease as $N^{-1/2}$. (This is evident in Figure 5.1, in which the short time oscillations of the energy are larger for the alanine dipeptide than for the trpzip2 system.) Fluctuations of size $\delta E/E$ will be less likely by a factor of $N^{-1/2}$, and the time spent waiting for these fluctuations increases. The difference in $N^{1/2}$ between the trpzip2 and the alanine dipeptide systems is about a factor of two, consistent with the factor of two difference in the τ values.

These results are encouraging and show that the system can be driven at reasonable time scales, from 20 to 40 ps, for a large temperature difference (120 K). For the REDS method with the same temperature scaling and the same alanine dipeptide system, λ varies from 0 to 1 over a time scale of about 20 ps (See Figure 1 of Reference [218]).This agrees well with the REDS2 value for τ. The time scale for λ dynamics is determined by energy fluctuations, which act as a force to move λ, and the choice of a mass for the λ variable. This means that under the influence of the energy fluctuations of the system, λ can vary from 0 to 1 on the same time scale as it can be driven using the REDS2 method. Any faster than this and the system will be out of equilibrium.

The way in which energy fluctuations propagate is different between conventional RE and REDS and between RE and REDS2. In conventional RE, if there is a fluctuation to a lower-energy structure for the high-temperature replica, that structure will tend to be exchanged with that of the replica at a lower temperature, as determined by the RE Metropolis criteria. How far that structure moves through the replicas depends on how its energy compared to that of the other replicas. In REDS, the structure will propagate downward by λ dynamically changing from zero to one (if $T_A<T_B$), which will happen if the force on λ moves it in that direction. The force is due to the difference in the energy of that structure and the biasing potential, which has been parameterized to represent an average energy for that value of λ. So for both RE and REDS, movement of a structure from high to low temperature first requires a fluctuation to a low-energy structure for the high-temperature replica, then a comparison of that energy with the energy of other replicas or with the biasing potential. In the REDS2 method, the energy of the structure is not used to propagate λ. The propagation is driven and the energy fluctuations are induced by the driven potential. The energy is used to accept swaps, using Equation 5.9, but if λ equals one, the swap will be accepted with probability one because Δ_{NM} will equal zero. If structure is out of equilibrium, either because it has been driven too fast or because it has gotten caught in a local minimum, then it will be accepted regardless of its energy at $\lambda = 1$.

This is illustrated in Figure 5.2 (A), in which the system is out of equilibrium and swaps are attempted every 0.1 ps. The swap at t=$\tau/2$ (when λ equals 1) is accepted even though the scaled replica has appreciably higher energy than the unscaled replica. The next

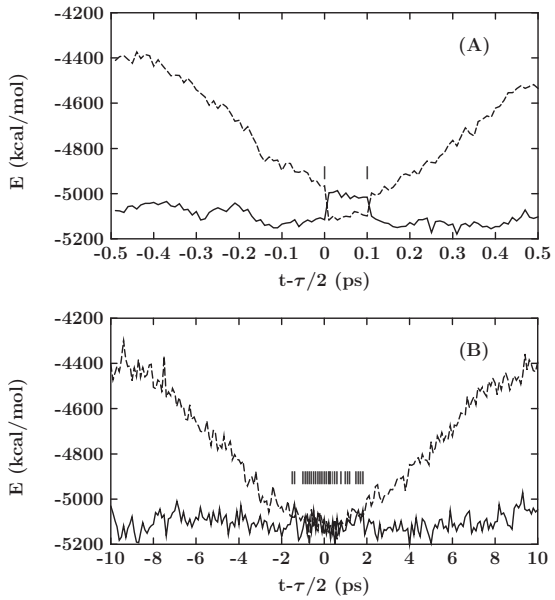

Figure 5.2: Energy versus time for two replicas of the alanine dipeptide system, with the T = 300 K (solid line) and the driven replica (T_A = 300 K,T_B = 420 K, and T_M = 350 K) with (A) τ = 1 ps and (B) τ = 20 ps. Vertical lines indicate the points at which exchanges were accepted.

attempt is also accepted, which removes the high-energy structure from the 300 K replica and after that, because λ is not equal to one, swaps will not be accepted with the higher energy configuration. By taking frequent swap attempts, these structures out of equilibrium will be eliminated. Of course, the structure will be retained for the duration of a swap attempt (here 0.1 ps) and will make an incorrect contribution to ensemble averages at this temperature, even if it is for a small time. If the driven replica is in equilibrium, then swaps will be accepted not only when t=$\tau/2$, but also for a range of time when the energies of the two replicas are close, as shown in Figure 5.2 (B). In this trajectory, 27 swaps are accepted over about a 4-ps interval, as indicated by the vertical lines, giving an acceptance ratio of about 50% over the interval. When t is between $\tau/2$ –0.6 and $\tau/2$+0.6 ps, every swap is accepted. There is an equal chance that either configuration eventually ends up at the lower

temperature, depending on whether an odd or even number of swaps is accepted during this interval. On the other hand, if the system is driven out of equilibrium, the higher energy configuration will not end up at the lower temperature, as long as more than the one swap attempt when λ equals 1 is made.

A good choice of the exchange frequency is important with the REDS2 method. For conventional RE, any calculated properties should be independent of the exchange frequency, although some choices may lead to more optimal sampling.[239, 240, 241, 242, 243] For the REDS2 method, it important that the exchange frequency not be out of phase with the driven Hamiltonian, so that attempts are made when λ is near zero or one. In addition, during the interval when λ is near these extremes, more than one attempt would be advantageous, so the exchange frequency should be much less than the period for the driven Hamiltonian, $1/\tau$.

Once suitable values of τ were found, the performance of the REDS2 method can be examined for the alanine dipeptide and the trpzip2 systems, with conditions as described above. The REDS2 method should give the same distribution of energies and the same average energy as a function of temperature as conventional RE or other methods. It should also give the same distribution of structures. The distribution of energies at 298 K for the alanine dipeptide shows close agreement between REDS2 and RE for the total energy, as shown in Figure 5.3 (A). The distributions are essentially identical; the total energy is almost completely due to the water interactions, so this agreement shows just the water degrees of freedom are in equilibrium. Figure 5.3 (B) shows the distribution of the torsional energy, which comes from the peptide only and represents the slow degrees of freedom with the highest barriers. This also shows good agreement between REDS2 and RE, indicating that the torsional degree of freedom are also in equilibrium. The trpzip2 system shows good agreement for the total and torsional energy between the REDS2 and REDS methods (Figure 5.4), so for this larger system, the coordinates appear to be in equilibrium with the time-dependent potential, as well. Ensemble averages over a range of temperatures can be

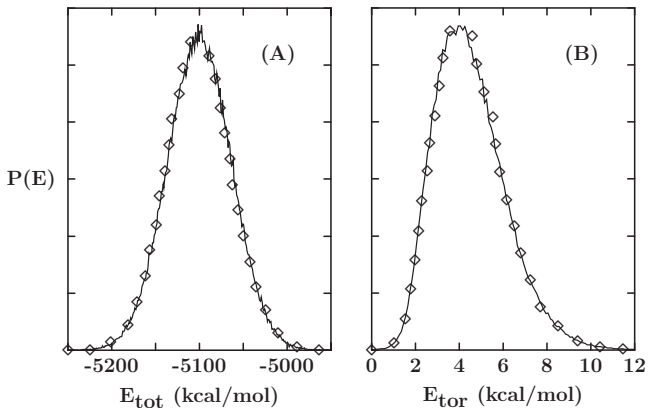

Figure 5.3: Distribution of energy at 298 K for the alanine dipeptide system for 5 replica REDS2 (solid lines) and 22 replica RE (diamonds) for (A) the total energy and (B) the torsional energy.

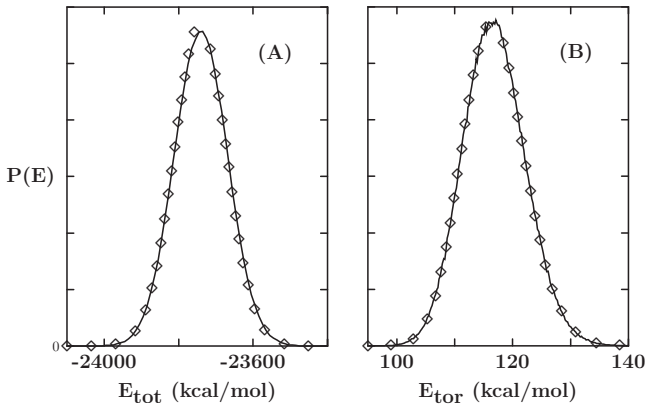

Figure 5.4: Distribution of energy at 298 K for the trpzip2 system for 10 replica REDS2 (solid lines) and 16 replica REDS (diamonds) for (A) the total energy and (B) the torsional energy.

calculated from a single REDS2 replica using Equation 5.15. Figure 5.5 compares the total and torsional energy from the scaled replicas of REDS2 with the RE results. This entire temperature range of 300 K is determined from the data for only two scaled replicas, which is being compared to the data from 22 conventional replicas. The two are in good agreement. Similar plots for the trpzip2 system are shown in Figure 5.6, comparing 10 replica REDS2 and 16 replica REDS. The agreement between the methods is close for both systems, indicating

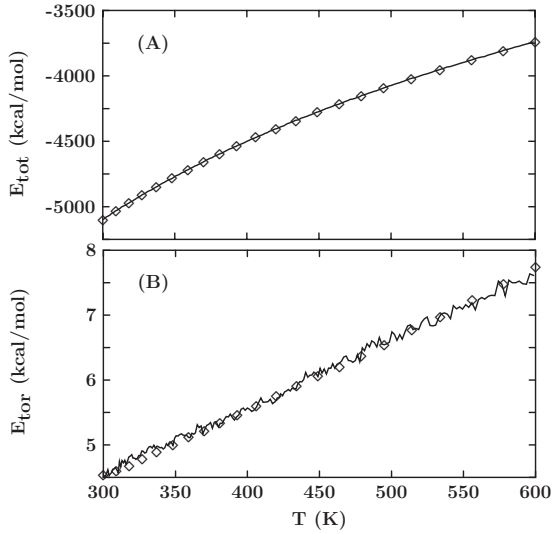

Figure 5.5: Average energy as a function of temperature for the alanine dipeptide system for 5 replica REDS2 (solid lines) and 22 replica RE (diamonds) for (A) the total energy and (B) the torsional energy.

that the scaled replicas are in equilibrium over the entire λ range. In addition to correct energies, the REDS2 method should also give the correct structures. The structures of the alanine dipeptide can be split up into four regions in the Ramachandran diagram.[244] The two most populated regions are $C7_{eq}$/C5 and $\alpha_R/\beta 2$. As mentioned previously, we started two sets of simulations with all replicas with one of the two regions. We can then examine the cumulative average of the population fraction, X, for each structure as a function of time. Figure 5.7 compares the population of the $C7_{eq}$/C5 region from the RE and REDS2 simulations. To make a fair comparison, the total simulation time for each method is used. This is equal to the simulation time for a single replica times the number of replicas, giving the total CPU time used by each method. The population fractions take a long time to

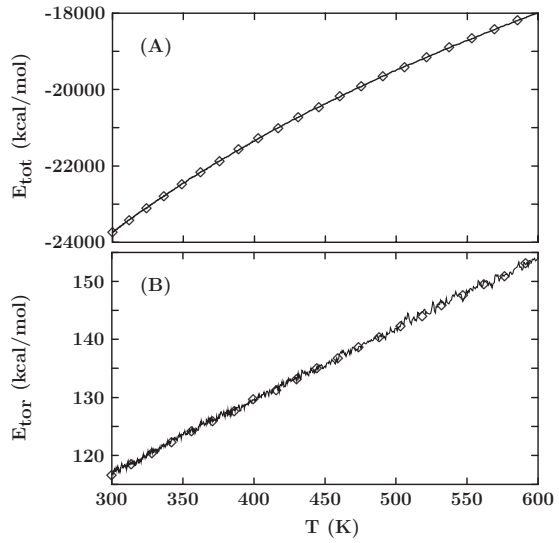

Figure 5.6: Average energy as a function of temperature for the trpzip2 system for 10 replica REDS2 (solid lines) and 16 replica REDS (diamonds) for (A) the total energy and (B) the torsional energy.

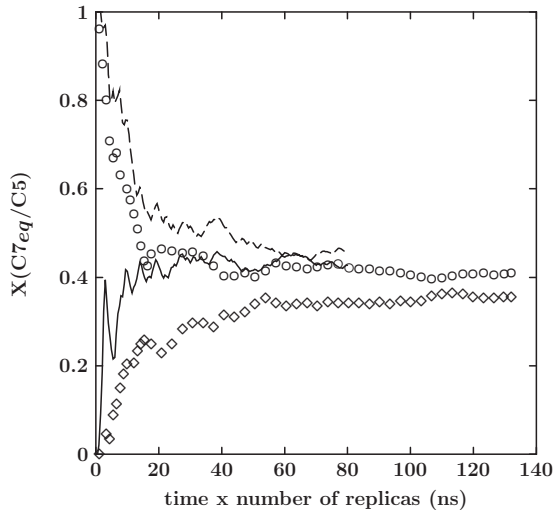

Figure 5.7: The population of the $C7_{eq}$/C5 structure for the alanine dipeptide at T = 298 K for 5 replica REDS2 (lines) and 22 replica RE (symbols). The diamonds and solid line represent the simulation that started in the $\alpha_R/\beta 2$ configuration and the circles and dashed line in the $C7_{eq}$/C5 structure.

converge (as is evident from Figure 5.7) because, rather than finding a single structure, the simulations need to make enough transitions among the structures to give the correct populations. The RE simulations starting from the different initial conditions are still not converged after 22 x 6 ns of total simulation time. The REDS2 simulations agree with each other more closely, after 5 x 14 ns, but it is not clear if the RE and REDS2 simulations are converging to the same value. Slow convergence is partially due to biases of the initial configurations, which are all either X($\alpha_R/\beta 2$) equal to 0 or 1. If we use only the second half of the data, assuming that we have reached equilibrium at this point and just need to accumulate enough transitions among structures, then we get good agreement between the two methods (Table 5.1). This agreement indicates that the REDS2 method is giving

Table 5.1: The populations of four structures of the alanine dipeptide, using data from the last half of the simulation.

Method	$C7_{eq}$/C5	$\alpha_R/\beta 2$	α_L	$C7_{ax}$
REDS2	0.40±0.04	0.57±0.04	0.025±0.008	0.003±0.002
RE	0.39±0.02	0.57±0.02	0.034±0.010	0.005±0.002

the correct distribution of structures for the alanine dipeptide system. (For the trpzip2 system, the simulations will have to go much longer than the times simulated here to achieve convergence for structural properties.)

The efficiency of RE is dependent on the time it takes to cycle from the highest temperature to the lowest. Figure 5.8 follows the temperature of a selected replica for 10 ns. The transitions among the temperatures follow a regular pattern, with rapid transitions between neighboring replicas at times when λ is near 0 and 1 followed by no transitions for a period of $\tau/2$ when λ is between 0 and 1 (τ equals 0.2 ns). An analysis of all the data from the trpzip2 simulations shows that it takes 5±1 ns for a replica to move from 273 to 600 K, which is consistent with Figure 5.8, where the replica goes from 273 to 600 and back in about 10 ns. This is at least as fast as conventional RE for the same system, as shown in Figure 2 of Reference[201]. For the alanine dipeptide system, the REDS2 method

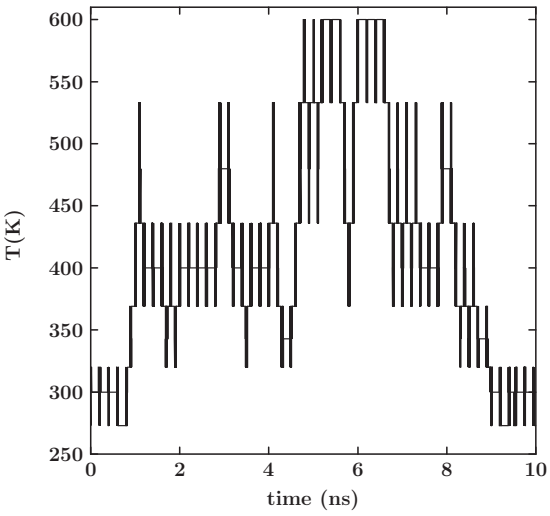

Figure 5.8: The temperature of a selected replica as a function of time for the trpzip2 system.

takes 0.16±0.02 ns to go from 300 to 600 K, about the same as conventional RE which takes 0.18±0.02 ns. This value for RE is faster than the value of 0.8±0.1 ns for the system reported previously.[218] That simulation attempted exchanges every 1 ps rather than 0.1 ps, as done here, demonstrating that smaller exchange frequencies may lead to more efficient sampling, as suggested elsewhere.[242] The replicas using REDS2 method move through temperature space about as fast as conventional RE, but with fewer replicas.

5.4 Conclusion

The REDS2 method can improve the efficiency of replica exchange by reducing the number of replicas, from 22 to 5 for the alanine dipeptide and about 60 to 10 for the trpzip2 system. The method combines conventionally simulated replicas at some temperatures with driven replicas using a time dependent potential. The driven replicas, in addition to bridging conventional replicas separated by large temperature differences, also give ensemble averages over a range of temperatures. The REDS2 method is easy to implement and easy to add to simulation packages like Amber and, because the driven replicas run at the same time as the conventional replicas, the method parallelizes as well as standard replica exchange. These features it has common with the REDS method.[218] The difference is that the REDS2

method does not require a biasing potential to ensure even sampling. Rather, it requires a single parameter, τ, which determines the time scale for the variations in the potential energy. The parameter needs to be chosen so that the system is in equilibrium, which can be determined by running for a period $\tau/2$ and seeing if the energy matches values from conventional simulations at the relevant temperatures (See Figure 5.1). If appropriate values for τ are used, then the REDS2 method successfully reproduces the energies and structures for the alanine dipeptide and the trpzip2 systems.

The method provides a solution to the problem caused by the poor system-size scaling of replica exchange. For conventional RE, as the number of degrees of freedom, f_s, increases, the number of replicas required to span the same temperature increases as approximately $f_s^{1/2}$.[198] For REDS2, the same number of replicas could, in principle, span the same temperature range, but the value of τ would need to increase. The alanine dipeptide and tripzip2 systems are different in size by a factor of 4.75 (mostly due to an increase in the number of water molecules) and the value of τ necessary to maintain equilibrium increases by about a factor of two. This implies that τ scales as $f_s^{1/2}$, consistent with how energy fluctuations depend on system size, as discussed above. This dependence of τ means it would take longer for replicas to cycle through the range of temperatures as f_s increases. Conventional RE would also take longer to cycle as f_s increases, because there are more replicas. The results of this study for the alanine dipeptide found that the cycle times for RE and REDS2 are about the same, if swap attempt frequencies for RE are optimal. The time scales for both methods are ultimately driven by the inherent energy fluctuations of the system, so, while it could be different for other systems, it makes sense that the cycle times are comparable and also that they have the same system size dependence, $f_s^{1/2}$. Taking all this together suggests that the REDS2 method scales better than conventional RE by a factor of $f_s^{1/2}$, from the increase in the number of replicas in RE. For large systems which can have average spacings of less than 5 K between replicas[199], REDS2 can be implimented to have spacing between replicas of about 50 K, as done here for the trpzip2 system.

An optimization of the temperature gaps spanned by the driven replicas and the form of the time dependence of the scaling variable λ was not attempted and better choices could be made. In this study, λ varies as $\sin^2(\pi t/\tau)$, which has the effect of moving λ more slowly at the end points (near 0 and 1). This allows for plenty of replica swaps at the end points, but it may be better to vary λ at a constant rate, e.g., by a triangle wave. Another possibility would be to pause the conventional replicas while the driven replicas are moving between the two limits when exchanges are unlikely. These variations may make the REDS2 method more efficient.

Acknowledgments

This work was supported from the National Science Foundation under contract number CHE-0611679. The computational resources of the Advanced Biomedical Computing Center at the National Cancer Institute in Frederick, MD are gratefully acknowledged. AJL gratefully acknowledges support from the State of Louisiana Board of Regents.

Chapter 6

Concluding Remarks

Our studies show the charge transfer increases as the surface or interface is approached, where hydrogen-bond asymmetry is greatest in water and aqueous systems. Results of the interfacial-charge-transfer studies indicate that charge transfer at the liquid/vapor interface will lead to a modest negative surface charge, whereas a positive interfacial charge is produced at the ice/liquid interface. Our collaboration with Collin Wick and the parameterization of his FLEX model proves the DCT model is simple geometry-dependent model that is easy to implement, applicable to a variety of potential models (polarizable, non-polarizable, rigid, flexible), and captures the essential physics of charge transfer.

Bibliography

[1] G Hura, J M Sorenson, R M Gleaser, and T Head-Gordon. Determining the role of hydration forces in protein folding. *J. Chem. Phys.*, 113:9140, 2000.

[2] J L F Abascal and C Vega. A general purpose model for the condensed phases of water: TIP4P/2005. *J. Chem. Phys.*, 123:234505, 2005.

[3] H W Horn, W C Swope, J W Pitera, J D Madera, T J Dick, G L Hura, and T Head-Gordon. Development of an improved four-site water model for biomolecular simulations: TIP4P-Ew. *J. Chem. Phys.*, 120:9665–9678, 2004.

[4] S W Rick. Simulations of ice and liquid water over a range of temperatures using the fluctuating charge model. *J. Chem. Phys.*, 114:2276–2283, 2001.

[5] G S Kell. Density, Thermal Expansivity, and Compressibility of Liquid Water from 0 to 150 degrees C: Correlations and Tables for Atmospheric Pressure and Saturation Reviewed and Expressed on 1968 Temperature Scale. *J. Chem. Eng. Data*, 20:97, 1975.

[6] W L Jorgensen, J Chandrasekhar, J D Madura, R W Impey, and M L Klein. Comparison of simple potential functions for simulating liquid water. *J. Chem. Phys.*, 79: 926–935, 1983.

[7] S W Rick, S J Stuart, and B J Berne. Dynamical fluctuating charge force fields: Application to liquid water. *J. Chem. Phys.*, 101:6141–6156, 1994.

[8] C G Malmberg and A A Maryott. *J. Res. Natl. Bur. Stand.*, 56:1, 1956.

[9] G S Kell. *Water–A Comprehensive Treatise*. Edited by F Franks, Plenum, New York, 1972.

[10] N E Dorsey. *Properties of Ordinary Water-Substance in all its Phases: Water Vapor, Water, and all the Ices*. Reinhold Publishing, New York, 1940.

[11] H R Pruppacher. Self-Diffusion Coefficient of Supercooled Water. *J. Chem. Phys.*, 56: 101, 1983.

[12] Y J Chung and S W Rick. The Effects of Charge Transfer Interactions on the Properties of Ice Ih. *J. Stat. Phys.*, 145:355–364, 2011.

[13] M P Allen and D J Tildesley. *Computer Simulation of Liquids*. Oxford University Press, Oxford, 1987.

[14] P Politzer, Z B Maksić, J S Murray, and K Sen. *Molecular Electrostatic Potentials: Concepts and Applications*. Elsevier Science B. V., Netherlands, 1996.

[15] R Alicki and M Fannes. *Quantum Dynamical Systems*. Oxford University Press, Oxford, 2001.

[16] A R Leach. *Molecular Modelling: Principles and Applications*. Pearson Education Limited, Essex, 2001.

[17] D Frenkel and B Smit. *Understanding Molecular Simulation–From Algorithms to Applications*. Academic Press, San Diego, CA, 2002.

[18] M J Field. *A Practical Introduction to the Simulation of Molecular Systems*. Cambridge University Press, New York, 2007.

[19] L Perera and M L Berkowitz. Many-body effects in molecular dynamics simulations of Na+(H2O)n and Cl–(H2O)n clusters. *J. Chem. Phys.*, 95:1954, 1991.

[20] S Sremaniak, L Perera, and M L Berkowitz. Enthalpies of formation and stabilization energies of Br– (H2O)n (n=1,2,..., 15) clusters. Comparisons between molecular dynamics computer simulations and experiment. *Chem. Phys. Lett.*, 218:377, 1994.

[21] T Chang and L X Dang. Recent Advances in Molecular Simulations of Ion Solvation at Liquid Interfaces. *Chem. Rev.*, 106:1305–1322, 2006.

[22] V Knecht, Z A Levine, and P T Vernier. Electrophoresis of neutral oil in water. *J. Colloid Interf. Sci.*, 352:223–231, 2010.

[23] Z Zhao, D M Rogers, and T L Beck. Polarization and charge transfer in the hydration of chloride ions. *J. Chem. Phys.*, 132:014502, 2010.

[24] A J Lee and S W Rick. The effects of charge transfer on the properties of liquid water. *J. Chem. Phys.*, 134:184507, 2011.

[25] A J Lee and S W Rick. Improving replica exchange using driven scaling. *J. Chem. Phys.*, 131:174113, 2009.

[26] P Ball. Water as an active constituent in cell biology. *Chem. Rev.*, 108:74–108, 2008.

[27] J Y Luo, W J Cui, P He, and Y Y Xia. Raising the cycling stability of aqueous lithium-ion batteries by eliminating oxygen in the electrolyte. *Nat. Chem.*, 2:760–765, 2009.

[28] C M Dobson. Protein folding and misfolding. *Nature*, 426:884–890, 2003.

[29] D Gidalevitz, Z Huang, and S A Rice. Protein folding at the air-water interface studied with x-ray reflectivity. *Proc. Natl. Acad. Sci.*, 96:2608–2611, 1999.

[30] Y Jung and R A Marcus. On the theory of organic catalysis on water. *J. Am. Chem. Soc.*, 129:5492, 2007.

[31] Y Jung and R A Marcus. Protruding interfacial OH groups and 'on-water' heterogeneous catalysis. *J. Phys.: Condens. Matter*, 22:284117, 2010.

[32] S Narayan, J Muldoon, M G Finn, V V Fokin, H C Kolb, and K B Sharpless. Unique Reactivity of Organic Compounds in Aqueous Suspension. *Agnew. Chem. Int. Ed.*, 44: 3275–3279, 2005.

[33] T D Kühne, T A Pascal, E Kaxiras, and Y Jung. New Insights into the Structure of the Vapor/Water Interface from Large-Scale First-Principles Simulations. *J. Chem. Phys. Lett.*, 2:105–113, 2011.

[34] G Quincke. *Ann. Phys. Chem.*, 113:513, 1861.

[35] J Carruthers. The electrophoresis of certain hydrocarbons and their simple derivatives as a function of pH. *Trans. Faraday Soc.*, 34:300, 1938.

[36] W Dickinson. The effect of pH upon the electrophoretic mobility of emulsions of certain hydrocarbons and aliphatic halides. *Trans. Faraday Soc.*, 34:140, 1941.

[37] A Graciaa, P Creux, and J Lachaise. Electrokinetics of gas bubbles. *Surf. Sci. Ser.*, 106:825, 2002.

[38] J K Beattie. Comment on 'Autoionization at the surface of neat water: Is the top layer pH neutral, basic, or acidic?' by R. Vácha, V. Buch, A. Milet, J. P. Devlin and P. Jungwirth, [*Phys. Chem. Chem. Phys.*, 2007, 9, 4736]. *Phys. Chem. Chem. Phys.*, 10:330–331, 2008.

[39] A Gray-Weale and J K Beattie. An explanation for the charge on water's surface. *Phys. Chem. Chem. Phys.*, 11:10994, 2009.

[40] J K Beattie, A M Djerdjev, and G G Warr. The surface of neat water is basic. *Faraday Discuss.*, 141:31–39, 2009.

[41] A Gray-Weale and J K Beattie. Comment on 'Behaviour of hydroxide at the water/vapor interface' [Chem. Phys. Lett. 474 (2009) 241]. *Chem. Phys. Lett.*, 481:22–24, 2009.

[42] V Knecht, H J Risselada, A E Mark, and S J Marrink. Electrophoretic mobility does not always reflect the charge on an oil droplet. *J. Colloid Interf. Sci.*, 381:477–486, 2008.

[43] P Jungwirth and D J Tobias. Specific Ion Effects at the Air/Water Interface. *Chem. Rev.*, 106:1259–1281, 2006.

[44] P Jungwirth and B Winter. Ions at Aqueous Interfaces: From Water Surface to Hydrated Proteins. *Annu. Rev. Phys. Chem.*, 59:343–366, 2008.

[45] V Buch, A Milet, R Vácha, P Jungwirth, and J P Devlin. Water surface is acidic. *Proc. Natl. Acad. Sci.*, 104:7342–7347, 2007.

[46] M K Petersen, S S Iyengar, T J F Day, and G A Voth. The Hydrated Proton at the Water Liquid/Vapor Interface. *J Phys. Chem. B*, 108:14804–14806, 2004.

[47] C D Cappa, J D Smith, B M Messer, R C Cohen, and R J Saykally. The Electronic Structure of the Hydrated Proton: A Comparative X-ray Absorption Study of Aqueous HCl and NaCl Solutions. *J. Phys. Chem. B*, 110:1166–1171, 2006.

[48] B Winter, M Faubel, R Vácha, and P Jungwirth. Behavior of hydroxide at the water/vapor interface. *Chem. Phys. Lett.*, 474:241–247, 2009.

[49] H Wang, E C Y Yan, E Borguet, and K B Eisenthal. Second harmonic generation from the surface of centrosymmetric particles in bulk solution. *Chem. Phys. Lett.*, 259: 15–20, 1996.

[50] E C Y Yan, Y Liu, and K B Eisenthal. New Method for Determination of Surface Potential of Microscopic Particles by Second Harmonic Generation. *J. Phys. Chem. B*, 102:6331–6336, 1998.

[51] K B Eisenthal. Second Harmonic Spectroscopy of Aqueous Nano- and Microparticle Interfaces. *Chem. Rev. Lett.*, 106:1462–1477, 2006.

[52] B Winter, M Faubel, R Vácha, and P Jungwirth. Reply to "Comments on Frontiers Article 'Behavior of hydroxide at the water/vapor interface'". *Chem. Phys. Lett.*, 481: 19–21, 2009.

[53] R Saykally. On the interfacial and dynamical properties of the hydroxide ion. *Chem. Phys. Lett.*, 481:1, 2009.

[54] E K Wilson. Storm in a Teacup. *Chem. Eng. News*, 88:35–36, 2010.

[55] R Vácha, S W Rick, P Jungwirth, A G F de Beer, H B de Aguiar, J-S Samson, and S Roke. The orientation and charge of water at the hydrophobic oil droplet-water interface. *J. Am. Chem. Soc.*, 133:10204–10210, 2011.

[56] E Schrödinger. Quantisierung ales eigenwertproblem. *Ann. Phys.*, 79:361, 1926.

[57] M Griebel, S Knapek, and G Zumbusch. *Numerical Simulations in Molecular Dynamics*. Springer, New York, 2000.

[58] M Born and J R Oppenheimer. Zur quantentheorie der molekeln. *Ann. Physik*, 84: 457, 1927.

[59] W D Cornell, P Cieplak, C I Bayly, I R Gould, K M Merz, Jr., D M Ferguson, D C Spellmeyer, T Fox, J W Caldwell, and P A Kollman. A second generation force field for the simulation of proteins, nucleic acids, and organic molecules. *J. Am. Chem. Soc.*, 117:5197, 1995.

[60] H J C Berendsen, J P M Postma, W F van Gunsteren, and J Hermans. *Intermolecular Forces*. Reidel, Dordrecht, 1981.

[61] H J C Berendsen, J R Grigera, and T P Straatsma. The missing term in effective pair potentials. *J. Phys. Chem.*, 91:6269, 1987.

[62] K Kitaura and K Morokuma. A new energy decomposition scheme for molecular interactions within the Hartree-Fock approximation. *Int. J. Quantum Chem.*, 10:325–340, 1976.

[63] A E Reed and F Wienhold. Natural bond orbital analysis of near-Hartree-Fock water dimer. *J. Chem. Phys.*, 78:4066–4073, 1982.

[64] W J Stevens and W H Fink. Frozen fragment reduced variational space analysis of hydrogen bonding interactions. Applications to the water dimer. *Chem. Phys. Lett.*, 139:15–22, 1987.

[65] W Chen and M S Gordon. Energy decomposition analysis for many-body interaction and applications to water complexes. *J. Phys. Chem.*, 100:14316–14328, 1996.

[66] T K Ghanty, V N Staroverov, P K Koren, and E R Davidson. Is the hydrogen bond in water dimer and ice covalent? *J. Am. Chem. Soc.*, 122:1210–1214, 2000.

[67] J Korchowiec and T Uchimaru. New energy partitioning scheme based on the self-consistent charge and configuration method for subsystems: Application to water dimer system. *J. Chem. Phys.*, 112:1623–1633, 2000.

[68] E D Glendening. Natural energy decomposition analysis: Extension to density functional methods and analysis of cooperative effects in water clusters. *J. Phys. Chem. A*, 109:11936–11940, 2005.

[69] J-P Piquemal, A Marquez, O Parisel, and C Giessner-Prettre. A CSOV study of the difference between HF and DFT intermolecular interaction energy values: The importance of the charge transfer contribution. *J. Comput. Chem.*, 26:1052–1062, 2005.

[70] R Z Khaliullin, A T Bell, and M Head-Gordon. Electron donation in the water-water hydrogen bond. *Chem. Eur. J.*, 15:851–855, 2009.

[71] A J Stone and A J Misquitta. Charge-transfer in Symmetry-Adapted Perturbation Theory. *Chem. Phys. Lett.*, 473:201–205, 2009.

[72] O Gálvez, P C Gómez, and L F Pacios. Variation with the intermolecular distance of properties dependent on the electron density in hydrogen bond dimers. *J. Chem. Phys.*, 115:11166–1184, 2001.

[73] P-O Åstrand, K Ruud, K V Mikkelsen, and T Helgaker. Atomic charges of the water molecule and the water dimer. *J. Phys. Chem. A*, 102:7686–7691, 1998.

[74] A van der Vaart and K M Merz, Jr. The role of polarization and charge transfer in the solvation of biomolecules. *J. Am. Chem. Soc.*, 121:9182–9190, 1999.

[75] M Dal Peraro, S Raugel, P Carloni, and M L Klein. Solute-solvent charge transfer in aqueous solution. *ChemPhysChem*, 6:1715–1718, 2005.

[76] A V Marenich, R M Olson, A C Chamberlin, C J Cramer, and D G Truhlar. Polarization effects in aqueous and nonaqueous solutions. *J. Chem. Theory Comput.*, 3: 2055–2067, 2007.

[77] Z Zhao, D M Rogers, and T L Beck. Polarization and charge transfer in the hydration of chloride ions. *J. Chem. Phys.*, 132:014502, 2010.

[78] S Varma and S B Rempe. Multi-body effects in ion binding and selectivity. *Biophys. J.*, 99:3394, 2010.

[79] W H Thompson and J T Hynes. Frequency shifts in the hydrogen-bonded OH stretch in halide-water clusters: The importance of charge transfer. *J. Am. Chem. Soc.*, 122: 6278–6286, 2000.

[80] W H Robertson, M A Johnson, E M Myshakin, and K D Jordon. Isolating the Charge-Transfer Component of the Anionic H Bond Via Spin Suppression of the Intracluster Proton Transfer Reaction in the NO^-.H2O Entrance Channel Complex. *J. Phys. Chem. A*, 106:10010–10014, 2002.

[81] S G Ramesh, S Re, and J T Hynes. Charge transfer and OH vibrational frequency shifts in nitrate-water clusters. *J. Phys. Chem. A*, 112:3391–3398, 2008.

[82] P Coppens. Direct evaluation of the charge transfer in the tetrathiafulvalene-tetracynanoquinodimethane (TTF-TCNQ) complex at 100 K by numerical integration of X-ray diffraction amplitudes. *Phys. Rev. Lett.*, 35:98–100, 1975.

[83] E D Stevens and P Coppens. Experimental density distributions of hydrogen bonds. High resolution study of alpha-oxalic acid dihydrate at 100 K. *Acta. Cryst.*, 36:1864–1876, 1980.

[84] L Belpassi, F Tarantelli, F Pirani, P Candori, and D Cappelletti. Experimental and theoretical evidence of charge transfer in weakly bound complexes of water. *Phys. Chem. Chem. Phys.*, 11:9970, 2009.

[85] Y Li, L Liu, and J M Farrar. Vibrational-Rotational Energy Distributions in the Reaction O– + D2 yields OD + D–. *J. Phys. Chem. A*, 113:15233, 2009.

[86] L Belpassi, M L Reca, F Tarantelli, L F Roncaratti, F Pirani, D Cappelletti, A Faure, and Y Scribano. Charge-Transfer Energy in the Water-Hydrogen Molecular Aggregate Revealed by Molecular-Beam Scattering Experiments, Charge Displacement Analysis, and *ab Initio* Calculations. *J. Am. Chem. Soc.*, 132:13046–13058, 2010.

[87] C W David. A variable charge central force model for water and its ionic dissociation products. *J. Chem. Phys.*, 104:7255–7260, 1996.

[88] C Millot, J-C Millot, J-C Soetens, M T C Martins Costa, M P Hodges, and A J Stone. Revised anisotropic site potentials for the water dimer and calculated properties. *J. Phys. Chem. A*, 102:754–770, 1998.

[89] A C T van Diun, S Dasgupta, F Lorant, and W A Goddard, III. ReaxFF: A reactive force field for hydrocarbons. *J. Phys. Chem. A*, 105:9396–9409, 2001.

[90] K Honda. An effective potential function with enhanced charge-transfer-type interaction for hydrogen-bonding liquids. *J. Chem. Phys.*, 117:3558–3569, 2002.

[91] R Chelli, V Schettino, and P Procacci. Comparing polarizable force fields to *ab initio* calculations reveals nonclassical effects in condensed phases. *J. Chem. Phys.*, 122: 234107, 2005.

[92] R Chelli, M Pagliai, P Procacci, G Cardini, and V Schettino. Polarization response of water and methanol investigated by a polarizable force field and density functional theory calculations: Implications for charge transfer. *J. Chem. Phys.*, 122:074504, 2005.

[93] J-P Piquemal, H Chevreau, and N Gresh. Toward a Separate Reproduction of the Contributions to the HF and DFT Intermolecular Interaction Energies by Polarizable Molecular Mechanics with SIBFA Potential. *J. Chem. Theory and Comput.*, 3:824–837, 2007.

[94] R Kumar, F F Wang, G R Jenness, and K D Jordan. A second generation distributed point polarizable water model. *J. Chem. Phys.*, 132:014309, 2010.

[95] T G A Youngs and C Hardacre. Application of static charge transfer within an ionic-liquid force field and its effect on structure and dynamics. *ChemPhysChem*, 9:1548–1558, 2008.

[96] J Schmidt, C Krekeler, F Dommert, Y Zhao, R Berger, L Delle Site, and C Holm. Ionic charge reduction and atomic partial charges from first-principles calcuations of 1,3-dimethylimidazolium chloride. *J. Phys. Chem. B*, 114:6150–6155, 2010.

[97] F H Stillinger and C W David. Polarization model for water and its ionic dissociation products. *J. Chem. Phys.*, 69:1473–1484, 1978.

[98] T P Lybrand and P A Kollman. Water-water and water-ion potential functions including terms for many-body effects. *J. Chem. Phys.*, 83:2923–2933, 1985.

[99] J A C Rullman and P T van Duijnen. A polarizable water model for calculation of hydration energies. *Molec. Phys.*, 63:451–475, 1988.

[100] M Sprik and M L Klein. A polarizable model for water using distributed charge sites. *J. Chem. Phys.*, 89:7556–7560, 1988.

[101] P Ahlström, A Wallqvist, S Engström, and B Jönsson. A molecular dynamics study of polarizable water. *Mol. Phys.*, 68:563–581, 1989.

[102] P Cieplak, P A Kollman, and T P Lybrand. A new water potential including polarization: application to gas-phase, liquid, and crystal properties of water. *J. Chem. Phys.*, 92:6755–6760, 1990.

[103] S Kuwajima and A Warshel. Incorporating electric polarizabilities in water-water interaction potentials. *J. Phys. Chem.*, 94:460–466, 1990.

[104] S-B Zhu, S Singh, and G W Robinson. A new flexible/polarizable water model. *J. Chem. Phys.*, 95:2791–2799, 1991.

[105] A Wallqvist and B J Berne. Effective potentials for liquid water using polarizable and nonpolarizable models. *J. Phys. Chem.*, 97:13841–13851, 1993.

[106] D N Bernardo, Y Ding, K Krogh-Jespersen, and R M Levy. An anisotropic polarizable water model: Incorporation of all-atom polarizabilities into molecular mechanics force fields. *J. Phys. Chem.*, 98:4180–4187, 1994.

[107] J W Caldwell and P A Kollman. Structure and Properties of Neat Liquids Using Nonadditive Molecular Dynamics: Water, Methanol, and *N*-Methylacetamide. *J. Phys. Chem.*, 99:6208–6219, 1995.

[108] I M Svishchev, P G Kusalik, P G Wang, and R J Boyd. Polarizable point-charge model for water: Results under normal and extreme conditions. *J. Chem. Phys.*, 105: 4742–4750, 1996.

[109] A A Chialvo and P T Cummings. Engineering a simple polarizable model for the molecular simulation of water applicable over wide ranges of state conditions. *J. Chem. Phys.*, 105:8274–8281, 1996.

[110] L X Dang and T-M Chang. Molecular dynamics study of water clusters, liquid, and liquid-vapor interface of water with many-body potentials. *J. Chem. Phys.*, 106:8149–8159, 1997.

[111] B Chen, J Xing, and J I Siepmann. Development of polarizable water force fields for phase equilibria calculations. *J. Phys. Chem. B*, 104:2391–2401, 2000.

[112] H A Stern, F Rittner, B J Berne, and R A Friesner. Combined fluctuating charge and polarizable dipole models: Application to a five-site water potential function. *J. Chem. Phys.*, 115:2237–2251, 2001.

[113] P Ren and J W Ponder. Polarizable atomic multipole water model for molecular mechanics simulation. *J. Phys. Chem. B*, 107:5933–5947, 2003.

[114] G Lamoureux, A D MacKerell, and B Roux. A simple polarizable model of water based on classical Drude oscillators. *J. Chem. Phys.*, 119:5185–5197, 2003.

[115] H Yu and W F van Gunsteren. Charge-on-spring polarizable water models revisited: From water clusters to liquid water to ice. *J. Chem. Phys.*, 118:11225–11236, 1996.

[116] G Lamoureux, E Harder, I V Vorobyov, B Roux, and A D MacKerell, Jr. A polarizable model of water for molecular dynamics simulations of biomolecules. *J. Chem. Phys.*, 418:245–249, 2006.

[117] K Watanabe and M L Klein. Effective pair potentials and the properties of water. *Chem. Phys.*, 131:157–167, 1989.

[118] D van der Spoel, P van Maaren, and H J C Berendsen. A systematic study of water models for molecular simulation: Derivation of water models optimized for use with a reaction field. *J. Chem. Phys.*, 108:10220–10230, 1998.

[119] A Glatätti, X Daura, and W F van Gunsteren. Derivation of an improved simple point charge model for liquid water: SPC/A and SPC/L. *J. Chem. Phys.*, 116:9811–9828, 2002.

[120] D J Price and C L Brooks, III. A modified TIP3P water potential for simulation with Ewald summation. *J. Chem Phys.*, 121:10096, 2004.

[121] S W Rick. A reoptimization of the five-site water potential (TIP5P) for use with Ewald sums. *J. Chem. Phys.*, 120:6085–6093, 2004.

[122] J L F Abascal, E Sanz, R G Fernández, and C Vega. A potential model for the study of ices and amorphous water: TIP4P/Ice. *J. Chem. Phys.*, 122:234511, 2005.

[123] A K Rappé and W A Goddard, III. Charge equilibration for molecular dynamics simulations. *J. Phys. Chem.*, 95:3358–3363, 1991.

[124] J Chen and T J Martinez. QTPIE: Charge transfer with polarization current equalization. A fluctuating charge model with correct asymptotics. *Chem. Phys. Lett.*, 438: 315–320, 2007.

[125] L Došen-Mićović, D Jeremić, and N L Allinger. Treatment of electrostatic effects within the molecular mechanics method. *J. Am. Chem. Soc.*, 105:1716–1722, 1983.

[126] H A Stern, G A Kaminski, J L Banks, R Zhou, B J Berne, and R A Friesner. Fluctuating charge, polarizable dipole, and combined models: Parameterization from *ab initio* quantum chemistry. *J. Phys. Chem. B*, 103:4730–4737, 1999.

[127] S A Clough, Y Beers, G P Klein, and L S Rothman. Dipole moment of water from Stark measurements of H2O, HDO, and D2O. *J. Chem. Phys.*, 59:2254, 1973.

[128] W L Jorgensen and J Tirado-Rives. Potential energy functions for atomic-level simulations of water and organic and biomolecular systems. *Proc. Natl. Acad. Sci.*, 102: 6665–6670, 2005.

[129] M W Mahoney and W L Jorgensen. A five-site model for liquid water and the reproduction of the density anomaly by rigid, nonpolarizable potential functions. *J. Chem. Phys.*, 112:8910–8922, 2000.

[130] P Ren and J W Ponder. Temperature and Pressure Dependence of the AMOEBA Water Model. *J. Phys. Chem. B*, 108:13427, 2004.

[131] S W Rick and A D J Haymet. Dielectric constant and proton order and disorder in ice Ih Monte Carlo computer simulations. *J. Chem. Phys.*, 118:9291, 2003.

[132] S W Rick. Simulations of proton order and disorder in ice Ih. *J. Chem. Phys.*, 122: 094504, 2005.

[133] W F Murphy. The Rayleigh depolarization ratio and rotational Raman spectrum of water vapor and the polarizability components for the water molecule. *J. Chem. Phys.*, 67:5877, 1977.

[134] A D Buckingham. A Theory of the Dielectric Polarization of Polar Substances. *Proc. Roy. Soc. London Ser. A*, 238:235, 1956.

[135] H Nada and J P van der Eerden. An intermolecular potential model for the simulation of ice and water near the melting point: A six-site model of H2O. *J. Chem. Phys.*, 118:7401, 2003.

[136] P Jedlovszky and R Vallauri. Temperature dependence of thermodynamic properties of a polarizable potential model of water. *Molec. Phys.*, 97:1157–1163, 1999.

[137] W L Jorgensen and C Jensen. Temperature dependence of TIP3P, SPC, and TIP4P water from NPT Monte Carlo simulations: Seeking temperatures of maximum density. *J. Comp. Chem.*, 19:1179–1186, 1998.

[138] L A Báez and P Clancy. Existence of a density maximum in extended simple point charge water. *J. Chem. Phys.*, 101:9837–9840, 1994.

[139] S Harrington, P H Poole, F Sciortino, and H E Stanley. Equation of state of supercooled water simulated using the extended simple point charge intermolecular potential. *J. Chem. Phys.*, 107:7443–7450, 1997.

[140] I-F W Kuo and C J Mundy. An *Ab Initio* Molecular Dynamics Study of the Aqueous Liquid-Vapor Interface. *Science*, 303:658–660, 2004.

[141] I-F W Kuo, C J Mundy, B L Eggimann, M J McGrath, J I Siepmann, B Chen, J Vieceli, and D J Tobias. Structure and Dynamics of the Aqueous Liquid/Vapor Interface: A Comprehensive Particle-Based Simulation Study. *J Phys. Chem. B*, 110:3738–3746, 2006.

[142] C D Wick, I-F W Kuo, C J Mundy, and X L Dang. The Effect of Polarizability for Understanding the Molecular Structure of Aqueous Interfaces. *J. Chem. Theory Comput.*, 3:2002–2010, 2007.

[143] R Vácha, O Marsalek, A P Willard, D J Bonthuis, R R Netz, and P Jungwirth. Charge Transfer between Water Molecules As the Possible Origin of the Observed Charging at the Surface of Pure Water. *J. Phys. Chem. Lett.*, 3:107–111, 2011.

[144] V P Sokhan and D J Tildesley. The free surface of water: molecular orientation, surface potential and nonlinear susceptibility. *Mol. Phys.*, 92:625, 1997.

[145] B C Garrett, G K Schenter, and A Morita. Molecular Simulations of the Transport of Molecules across the Liquid/Vapor Interface of Water. *Chem. Rev.*, 106:1355–1374, 2006.

[146] A Perry, C Neipert, B Space, and P B Moore. Theoretical Modeling of Interface Specific Vibrational Spectroscopy: Methods and Applications to Aqueous Interfaces. *Chem. Rev.*, 106:1234–1258, 2006.

[147] G L Richmond. Molecular Bonding and Interactions at Aqueous Surfaces as Probed by Vibrational Sum Frequency Spectroscopy. *Chem. Rev.*, 102:2693–2724, 2002.

[148] S Gopalakrishnan, D F Liu, H C Allen, M Kuo, and M J Shultz. Vibrational Spectroscopic Studies of Aqueous Interfaces: Salts, Acids, Bases, and Nanodrops. *Chem. Rev.*, 106:1155–1175, 2006.

[149] P B Petersen and R J Saykally. On the nature of ions at the liquid water surface. *Annu. Rev. Phys. Chem.*, 57:333–364, 2006.

[150] M Takahashi. Zeta Potential of Microbubbles in Aqueous Solutions: Electrical Properties of the Gas?Water Interface. *J. Phys. Chem. B*, 109:21858, 2005.

[151] H Takahashi, K Maruyama, Y Karino, A Morita, M Nakano, P Jungwirth, and N Matubayasi. Energetic Origin of Proton Affinity to the Air/Water Interface. *J. Phys. Chem. B*, 115:4745–4751, 2011.

[152] L W Zilch, J Maze, J W Smith, G E Ewing, and M F Jarrold. Charge Separation in the Aerodynamic Breakup of Micrometer-Sized Water Droplets. *J. Phys. Chem. A*, 112:13352, 2008.

[153] A E Howard, U C Singh, M Billeter, and P A Kollman. Many-body potential for molecular interactions. *J. Am. Chem. Soc.*, 110:6984, 2007.

[154] H A McTaggart. *Philosophical Magazine*, 27:297, 1924.

[155] A Graciaa, G Morel, P Saulner, J Lachaise, and R S Schechter. The Zeta-Potential of Gas Bubbles. *J. Colloid Interf. Sci.*, 172:131–136, 1995.

[156] P Saulner, P Bouriat, G Morel, J Lachaise, and A Graciaa. Zeta Potential of Air Bubbles in Solutions of Binary Mixtures of Surfactants (Monodistributed Nonionic/Anionic Surfactant Mixtures). *J. Colloid Interf. Sci.*, 200:81–85, 1998.

[157] K G Marinova, R G Alargova, N D Denkov, O D Velev, D N Petsev, I B Ivanov, and R P Borwankar. Charging of Oil/Water Interfaces Due to Spontaneous Adsorption of Hydroxyl Ions. *Langmuir*, 12:2045, 1996.

[158] P Creux, J Lachaise, A Graciaa, J K Beattie, and A M Djerdjev. Strong Specific Hydroxide Ion Binding at the Pristine Oil/Water and Air/Water Interfaces. *J. Phys. Chem. B*, 113:14146–14150, 2009.

[159] M A Wilson, A Pohorille, and L R Pratt. Surface potential of the water liquid-vapor interface. *J. Chem. Phys.*, 88:3281–3285, 1988.

[160] L X Dang and T-M Chang. Molecular Mechanism of Ion Binding to the Liquid/Vapor Interface of Water. *J. Phys. Chem. B*, 106:235–238, 2002.

[161] C D Wick, L X Dang, and P Jungwirth. Simulated surface potentials at the vapor-water interface for the KCl aqueous electrolyte solution. *J. Chem. Phys.*, 125:024706, 2006.

[162] C D Wick and L X Dang. Molecular Dynamics Study of Ion Transfer and Distribution at the Interface of Water and 1,2-Dichloroethane. *J. Phys. Chem. C*, 112:647, 2008.

[163] K R Wilson, R D Schaller, D T Co, R J Saykally, B S Rude, T Catalano, and J D Bozek. Surface relaxation in liquid water and methanol studied by x-ray absorption spectroscopy. *J. Chem. Phys.*, 117:7738–7744, 2002.

[164] K A Motakabbir and M L Berkowitz. Liquid-vapor interface of TIP4P water: comparison between a polarizable and a nonpolarizable model. *Chem. Phys. Lett.*, 176:61–66, 1991.

[165] M D Baer, C J Mundy, M J McGrath, I-F W Kuo, J I Siepmann, and D J Tobias. Re-examining the properties of the aqueous vapor-liquid interface using dispersion corrected density functional theory. *J. Chem. Phys.*, 135:124712, 2011.

[166] C D Wick. Hydronium Behavior at the Air-Water Interface with a Polarizable Multistate Empirical Valence Bond Model. *J. Phys. Chem. C*, 116:4026–4038, 2012.

[167] A L Maniero, M Brustolon, M F Ottaviani, P Sgarabotto, and L Greci. EPR and ENDOR study on mixed crystals of an indolinone nitroxide radical and the isoelectronic ketone. I. X-ray structure of pure components and ENDOR of isolated radicals in mixed crystals. *Mol. Phys.*, 73:1, 1991.

[168] J Sala, E Gurdia, and M Masia. The polarizable point dipoles method with electrostatic damping: Implementation on a model system. *J. Chem. Phys.*, 133:234101, 2010.

[169] B T Thole. Molecular polarizabilities calculated with a modified dipole interaction. *Chem. Phys.*, 59:341–350, 1981.

[170] J Kolafa. Time-reversible always stable predictor-corrector method for molecular dynamics of polarizable molecules. *J. Comput. Chem.*, 25:335–342, 2004.

[171] H C Andersen. Molecular-dynamics simulations at constant pressure and/or temperature. *J. Chem. Phys.*, 72:2384–2394, 1980.

[172] J P Ryckaert, G Ciccotti, and H J C Berendsen. Numerical integration of the Cartesian equations of motion of a system with constraints: Molecular dynamics of n-alkanes. *J. Comput. Phys.*, 23:327–341, 1977.

[173] U Essmann, L Perera, M L Berkowitz, T Darden, H Lee, and L G Pedersen. A smooth particle mesh Ewald method. *J. Chem. Phys.*, 103:8577–8593, 1995.

[174] D Eisenberg and W Kauzmann. *The Structure and Properties of Water*. Oxford University Press, New York and Oxford, 1969.

[175] K Krynicki, C D Green, and D W Sawyer. Pressure and temperature dependence of self-diffusion in water. *Faraday Discuss. Chem. Soc.*, 66:199–208, 1978.

[176] R Buchner, J Barthel, and J Stauber. The dielectric relaxation of water between 0 degrees C and 35 degrees C. *Chem. Phys. Lett.*, 306:57–63, 1999.

[177] F MacRitchie. *Chemistry at Interfaces*. Academic Press, San Diego, CA, 1990.

[178] F Chen and P E Smith. Simulated surface tensions of common water models. *J Chem Phys*, 126:221101, 2007.

[179] G Tammann. Ueber die Grenzen des festen Zustandes IV. *Ann. Phys.*, 307:1–31, 1900.

[180] L Pauling. *The Nature of the Chemical Bond*. Cornell University Press, Ithaca, NY, 1960.

[181] V F Petrenko. Study of the Surface of Ice, Ice/Solid and Ice/Liquid Interfaces with Scanning Force Microscopy. *J. Phys. Chem. B*, 101:6276–6281, 1997.

[182] V F Petrenko and R W Whitworth. *Physics of Ice*. Oxford University Press, Inc., New York, 2002.

[183] B J Murray, D A Knopf, and A K Bertram. The formation of cubic ice under conditions relevant to Earths atmosphere. *Nature*, 434:202, 2005.

[184] B J Murray and A K Bertram. Formation and stability of cubic ice in water droplets. *Phys. Chem. Chem. Phys.*, 8:186192, 2006.

[185] B J Murray and A K Bertram. Inhibition of solute crystallisation in aqueous H^+–NH_4^+–SO_4^2–H_2O droplets. *Phys. Chem. Chem. Phys.*, 10:32873301, 2008.

[186] J D Bernal and R H Fowler. A Theory of Water and Ionic Solution, with Particular Reference to Hydrogen and Hydroxyl Ions. *J. Chem. Phys.*, 1:515, 1933.

[187] L Pauling. The Structure and Entropy of Ice and of Other Crystals with Some Randomness of Atomic Arrangement. *J. Amer. Chem. Soc.*, 57:2680, 1935.

[188] D R Hamann. H_2O hydrogen bonding in density-functional theory. *Phys. Rev. B*, 55: R10157, 1997.

[189] J H Seinfeld and S N Pandis. *Atmospheric Chemistry and Physics–From Air Pollution to Climate Change*. John Wiley & Sons, Inc., Hoboken, NJ, 2006.

[190] A J Heymsfield and L J Donner. A Scheme for Parameterizing Ice-Cloud Water Content in General Circulation Models. *J. Atmos. Sci.*, 47:1865–1877, 1990.

[191] W Ostwald. *Z. Phys. Chem.*, 22:289, 1897.

[192] B Militzer and H F Wilson. New Phases of Water Ice Predicted at Megabar Pressures. *Phys. Rev. Lett.*, 105:195701, 2010.

[193] B Rowland and J P Devlin. Spectra of dangling OH groups at ice cluster surfaces and within pores of amorphous ice. *J. Chem. Phys.*, 94:812–813, 1991.

[194] B Rowland and N S Kadagathur and J P Devlin and T Feldman and *et al.* Infrared spectra of ice surfaces and assignment of surface-localized modes from simulated spectra of cubic ice. *J. Chem. Phys.*, 102:8328–8341, 1995.

[195] E R Batista, S S Xantheas, and H Jónsson. Multipole moments of water molecules in clusters and ice Ih from first principles calculations. *J. Chem. Phys.*, 109:6011–6015, 1999.

[196] P L Silvestrelli and M Parinello. Flexible simple point-charge water model with improved liquid-state properties. *J. Chem. Phys.*, 111:3572–3580, 1999.

[197] D J Earl and M W Deem. Parallel tempering: Theory, applications, and new perspectives. *Phys. Chem. Chem. Phys.*, 7:3910–3916, 2005.

[198] H Fukunishi, O Watanabe, and S Takada. On the Hamiltonian replica exchange method for efficient sampling of biomolecular systems: Application to protein structure prediction. *J. Chem. Phys.*, 116:9058–9067, 2002.

[199] J W Pitera, I Haque, and W C Swope. Absence of reptation in the high-temperature folding of the trpzip2 beta-hairpin peptide. *J. Chem. Phys.*, 124:141102, 2006.

[200] R Zhou, B J Berne, and R Germain. The free energy landscape for β hairpin folding in explicit water. *Proc. Natl. Acad. Sci. USA*, 98:14931, 2001.

[201] J Zhang, M Qin, and W Wang. Folding mechanism of beta-hairpins studied by replica exchange molecular simulations. *Proteins*, 62:672–685, 2006.

[202] S Yang, J N Onuchic, A E Garcia, and H Levine. Folding time predictions from all-atom replica exchange simulations. *J. Mol. Biol.*, 372:756–763, 2007.

[203] R Zhou and B J Berne. Smart walking: A new method for Boltzmann sampling of protein conformations. *J. Chem. Phys.*, 107:9185, 1997.

[204] I Andricioaei, J E Straub, and A F Voter. Smart darting Monte Carlo. *J. Chem. Phys.*, 114:6994, 2001.

[205] S Brown and T Head-Gordon. Cool walking: A new Markov chain Monte Carlo sampling method. *J. Comput. Chem.*, 24:68–76, 2002.

[206] X. Li, C P O'Brien, G Collier, N A Vellore, F. Wang, R A Latour, D A Bruce, and S J Stuart. An improved replica-exchange sampling method: Temperature intervals with global energy reassignment. *J. Chem. Phys.*, 127:164116, 2007.

[207] E Lyman and D M Zuckerman. Annealed importance sampling of peptides. *J. Chem. Phys.*, 127:065101, 2007.

[208] Y Sugita and Y Okamoto. Replica-exchange multicanonical algorithm and multicanonical replica-exchange method for simulating systems with rough energy landscapes. *Chem. Phys. Lett.*, 329:261–270, 2000.

[209] F Calvo and J P K Doye. Entropic tempering: A method for overcoming quasiergodicity in simulation. *Phys. Rev. E*, 63:010902, 2000.

[210] R Faller, Q Yan, and J J de Pablo. Multicanonical parallel tempering. *J. Chem. Phys.*, 116:5419–5423, 2002.

[211] M K Fenwick and F A Escobedo. Expanded ensemble and replica exchange methods for simulation of protein-like systems. *J. Chem. Phys.*, 119:11998–12010, 2003.

[212] A Mitsutake and Y Okamoto. Replica-exchange extensions of simulated tempering method. *J. Chem. Phys.*, 121:2491–2504, 2004.

[213] T W Whitfield, L Bu, and J E Straub. Generalized parallel sampling. *Physica A*, 305: 157–171, 2002.

[214] S Jang, S Shin, and Y Pak. Replica-exchange method using the generalized effective potential. *Phys. Rev. Lett.*, 91:058305, 2003.

[215] P Liu, B Kim, R A Friesner, and B J Berne. Replica exchange with solute tempering: A method for sampling biological systems in explicit water. *Proc. Natl. Acad. Sci. USA*, 102:13749–13754, 2005.

[216] P Liu, X Huang, R Zhou, and B J Berne. Hydrophobic Aided Replica Exchange: an Efficient Algorithm for Protein Folding in Explicit Solvent. *J. Phys. Chem. B*, 110: 19018–19022, 2006.

[217] S Kannan and M Zacharias. Enhanced sampling of peptide and protein conformations using replica exchange simulations with a peptide backbone biasing-potential. *Proteins*, 66:697–706, 2007.

[218] S W Rick. Replica exchange with dynamical scaling. *J. Chem. Phys.*, 126:054102, 2007.

[219] X Kong and C L Brooks, III. Lambda-dynamics: A new approach to free energy calculations. *J. Chem. Phys.*, 105:2414–2523, 1995.

[220] R M Lynden-Bell and J C Rasaiah. From hydrophobic to hydrophilic behavior: A simulation study of solvation entropy and free energy of simple solutes. *J. Chem. Phys.*, 107:1981–1991, 1997.

[221] Z. Guo, C L Brooks, III, and X Kong. Efficient and flexible algorithm for free energy calculations using the lambda-dynamics approach. *J. Phys. Chem. B*, 102:2032–2036, 1998.

[222] N F A van der Vegt and W J Briels. Efficient sampling of solvent free energies in polymers. *J. Chem. Phys.*, 109:7578–7582, 1998.

[223] U Börjesson and P H Hünenberger. Explicit solvent molecular dynamics at constant pH: Methodology and applications to small amines. *J. Chem. Phys.*, 114:9706–9719, 2001.

[224] M S Lee, F R Salsbury, and C L Brooks, III. Constant-pH molecular dynamics using continuous titration coordinates. *Proteins*, 56:738–752, 2004.

[225] J Khandogin and C L Brooks, III. Constant-pH molecular dynamics with proton tautomerism. *Biophysical J.*, 89:141–157, 2005.

[226] J B Abrams, L Rosso, and M E Tuckerman. Efficient and precise solvation free energies via alchemical adiabatic molecular dynamics. *J. Chem. Phys.*, 125:074115, 2006.

[227] C Predescu, M Predescu, and C V Ciobanu. On the efficiency of exchange in parallel tempering Monte Carlo simulations. *J. Phys. Chem. B*, 109:4189–4196, 2005.

[228] S Trebst, M Troyer, and U H E Hansmann. Optimized parallel tempering simulations of proteins. *J. Chem. Phys.*, 124:174903, 2006.

[229] N Rathore, M Chopra, and J J de Pablo. Optimal allocation of replicas in parallel tempering simulations. *J. Chem. Phys.*, 122:024111, 2005.

[230] A Kone and D A Kofke. Selection of temperature intervals for parallel-tempering simulations. *J. Chem. Phys.*, 122:206101, 2005.

[231] A G Cochran, N J Skelton, and M A Starovasnik. Tryptophan zippers: Stable, monomeric beta-hairpins. *Proc. Natl. Acad. Sci. USA*, 98:5578, 2001.

[232] N Metropolis, A W Rosenbluth, M N Rosenbluth, A N Teller, and E Teller. Equation of state calculations by fast computing machines. *J. Chem. Phys.*, 21:1087–1092, 1953.

[233] W L Jorgensen, D S Maxwell, and J Tirado-Rives. Development and Testing of the OPLS All-Atom Force Field on Conformational Energetics and Properties of Organic Liquids. *J. Am. Chem. Soc.*, 118:11225–11236, 1996.

[234] G A Kaminski, R A Friesner, J Tirado-Rives, and W L Jorgensen. Evaluation and Reparameterization of the OPLS-AA Force Field for Proteins via Comparison with Accurate Quantum Chemical Calculations on Peptides. *J. Phys. Chem. B*, 105:6474–6487, 2001.

[235] Y Sugita and Y Okamoto. Replica-exchange molecular dynamics method for protein folding. *Chem. Phys. Lett.*, 314:141–151, 1999.

[236] J M Wang, P Cieplak, and P A Kollman. How well does a restrained electrostatic potential (RESP) model perform in calculating conformational energies of organic and biological molecules? *J. Comput. Chem.*, 21:1049–1074, 2000.

[237] V. Hornak, R Abel, A Okur, B Strockbine, A Roitberg, and C Simmerling. Comparison of multiple amber force fields and development of improved protein backbone parameters. *Proteins*, 65:712–725, 2006.

[238] D A Case, T A Darden, T E Cheatham III, C L Simmerling, J Wang, R E Duke, R Luo, K M Merz, D A Pearlman, M Crowley, R C Walker, W Zhang, B Wang, S Hayik, A Roitberg, G Seabra, K F Wong, F Peasani, X Wu, S Brozell, V Tsui, H Gohlke, L Yang, C Tan, J Mongan, V Hornak, G Cui, P Beroza, D H Mathews, C Schafmeister, W S Ross, and P A Kollman. Amber 9, University of California, San Francisco, 2006.

[239] S B Opps and J Schofield. Extended state-space Monte Carlo methods. *Phys. Rev. E*, 63:056701, 2001.

[240] W Zhang, C Wu, and Y Duan. Convergence of replica exchange molecular dynamics. *J. Chem. Phys.*, 123:154105, 2005.

[241] X Periole and A E Mark. Convergence and sampling efficiency in replica exchange simulations of peptide folding in explicit solvent. *J. Chem. Phys.*, 126:014903, 2007.

[242] D Sindhikara, Y Meng, and A E Roitberg. Exchange frequency in replica exchange molecular dynamics. *J. Chem. Phys.*, 128:024103, 2008.

[243] M J Abraham and J E Gready. Ensuring mixing efficiency of replica-exchange molecular dyanmics simulations. *J. Chem. Theory Comput.*, 4:1119–1128, 2008.

[244] The $C7_{eq}$/C5 region is defined as $\phi < 0$ or $\phi > 130$ and $\psi < -110$ or $\psi > 80$; $\alpha_R/\beta 2$ is $\phi < 0$ or $\phi > 130$ and $-110 < \psi < 80$; α_L is $0 < \phi < 130$ and $-60 < \psi < 90$; and $C7_{ax}$ is $0 < \phi < 130$ and $\psi < -60$ or $\psi > 90$.

[245] L R Olano and S W Rick. Fluctuating charge normal modes: An algorithm for implementing molecular dynamics simulations with polarizable potentials. *J. Comput. Chem.*, 26:699, 2005.

Appendix

Supplementary Information for Chapter 3

I. Molecular dynamics with the TIP4P+DCT model. Because the charges depend on the positions of the particles, there is a charge-transfer contribution to the forces, given by

$$\left(\frac{\partial E}{\partial r_{i\alpha}}\right) = \left(\frac{\partial E_{LJEl}}{\partial r_{i\alpha}}\right)_Q + \left(\frac{\partial E_{CT}}{\partial r_{i\alpha}}\right) + \sum_{j=1}^{N}\sum_{\beta=1}^{3}\left(\frac{\partial (E_{LJEl}+E_{pol})}{\partial q_{j\beta}}\right)\left(\frac{\partial q_{j\beta}}{\partial r_{i\alpha}}\right), \tag{6.1}$$

where $(\partial E_{LJEl}/\partial r_{i\alpha})_Q$ is the force with constant charge from the Lennard-Jones and electrostatic energy, E_{LJEl}, which is the only contribution to the force for standard models. The contribution to the forces from the charge transfer energy is

$$\left(\frac{\partial E_{CT}}{\partial r_{i\alpha}}\right) = \sum_{j=1}^{N}(\mu_{CT}\delta Q_t + \eta_{CT}(N_d^j\delta Q_t))\delta Q_t\left(\frac{\partial N_d^j}{\partial r_{i\alpha}}\right). \tag{6.2}$$

The value of N_d^j depends on the oxygen position of molecules other than j and the hydrogen positions of molecule j. For oxygen atoms, we have

$$\left(\frac{\partial E_{CT}}{\partial r_{iO}}\right) = \sum_{j\neq i}(\mu_{CT}\delta Q_t + \eta_{CT}(N_d^j\delta Q_t))\delta Q_t\left(\frac{\partial N_d^j}{\partial r_{iO}}\right), \tag{6.3}$$

and for hydrogen atoms, with α indicating the two hydrogen atoms only,

$$\left(\frac{\partial E_{CT}}{\partial r_{i\alpha}}\right) = (\mu_{CT}\delta Q_t + \eta_{CT}(N_d^i\delta Q_t))\delta Q_t\left(\frac{\partial N_d^i}{\partial r_{i\alpha}}\right). \tag{6.4}$$

For the final term in Equation 6.1, we have

$$\left(\frac{\partial (E_{LJEl}+E_{pol})}{\partial q_{j\beta}}\right) = \sum_{j\neq i}\sum_{\alpha=1}^{3} q_{i\alpha}/r_{i\alpha j\beta} + \frac{(\mu_j-\mu_{gp})}{\alpha}\left(\frac{\partial \mu_j}{\partial q_{j\beta}}\right) \tag{6.5}$$

and

$$\left(\frac{\partial q_{j\beta}}{\partial r_{i\alpha}}\right) = Q(\beta,1)\left(\frac{\partial N_d^{j1}}{\partial r_{i\alpha}}\right) + Q(\beta,2)\left(\frac{\partial N_d^{j2}}{\partial r_{i\alpha}}\right) + Q(\beta,3)\left(\frac{\partial N_a^{j}}{\partial r_{i\alpha}}\right), \tag{6.6}$$

where the matrix Q gives the response of the charges to the number of hydrogen bonds, as given by Equation 3.6. (For simplicity, the long-ranged treatment of electrostatic interactions through Ewald sums is not given in Equations 3.9 and 6.5).

The derivatives of the hydrogen bond numbers are given by

$$\left(\frac{\partial N_d^{j\beta}}{\partial r_{i\alpha}}\right) = \begin{cases} 0 & i=j, \alpha=O \\ \sum_{k\neq j} N'(kO\cdots i\alpha)(r_{i\alpha}-r_{kO})/|r_{i\alpha}-r_{kO}| & i=j, \alpha\neq O \\ N'(iO\cdots j\beta)(r_{iO}-r_{k\beta})/|r_{iO}-r_{k\beta}| & i\neq j, \alpha=O \\ 0 & i\neq j, \alpha\neq O \end{cases} \tag{6.7}$$

and

$$\left(\frac{\partial N_a^{j}}{\partial r_{i\alpha}}\right) = \begin{cases} \sum_{k\neq j}\sum_{\beta=H1}^{H2} N'(iO\cdots k\beta)(r_{iO}-r_{k\beta})/|r_{iO}-r_{k\beta}| & i=j, \alpha=O \\ 0 & i=j, \alpha\neq O \\ 0 & i\neq j, \alpha=O \\ N'(jO\cdots i\alpha)(r_{i\alpha}-r_{jO})/|r_{i\alpha}-r_{jO}| & i\neq j, \alpha\neq O, \end{cases} \tag{6.8}$$

where β indicates the hydrogen atoms, with

$$N'(iO\cdots j\alpha) = \begin{cases} 0 & \mathrm{r}_{iOj\alpha} < \mathrm{r}_1 \\ -(1/2)[\pi/(r_2-r_1)]\sin(\pi(r_{iOj\alpha}-r_1)/(r_2-r_1)) & \mathrm{r}_1 < \mathrm{r}_{iOj\alpha} < \mathrm{r}_2 \\ 0 & \mathrm{r}_2 < \mathrm{r}_{iOj\alpha}\ . \end{cases} \tag{6.9}$$

The presented procedure for including charge transfer in non-polarizable models does not require much additional computational expense. For each molecular dynamics timestep, a few extra steps are necessary:

1. Once new positions are generated, the hydrogen bond variables, N_d^{i1}, N_d^{i2}, and N_a^i, are found from Equations 3.1, 3.2, and 3.7.

2. The charges are then found using Equation 3.6.

3. The energy and forces from the Lennard-Jones and Coulombic interactions are determined.

4. The polarization and charge transfer energies (Equations 3.5 and 3.8) are determined.

5. A final step involves adding the contribution to the forces from the position-dependent charges from Equation 6.1. This is done after step 3 because it requires the term, $\sum_{j\neq i}\sum_\alpha q_{i\alpha}/r_{i\alpha j\beta}$, in Equation 6.5, which can be calculated along the energy.

As previously mentioned, these extra steps are not computationally expensive because there are no additional intermolecular distances to be calculated and no self-consistent equations to be solved iteratively, or through other methods, as is the case with polarizable models.

II. Molecular dynamics with the TIP4P-FQ+DCT model. In the original versions of fluctuating charge models, the charges are given masses and propagated with Newton's equations of motion. For fluctuating charge water models, the extended Lagrangian technique was shown to work well, and standard 1-femtosecond time steps could be used.

Charge transfer introduces new timescales into the charge dynamics, and, consequently, the same extended Lagrangian method was not effective. This problem can be solved by a change of coordinates to charge normal modes.[245] The normal mode charges are

$$\begin{pmatrix} Q_{i1} \\ Q_{i2} \\ Q_{i3} \end{pmatrix} = \begin{pmatrix} 1 & 1 & 1 \\ 0 & 1 & -1 \\ -2/3 & 1/3 & 1/3 \end{pmatrix} \begin{pmatrix} q_{iO} \\ q_{iH1} \\ q_{iH2} \end{pmatrix}. \tag{6.10}$$

The first normal mode is simply the total charge, which is set equal to Q_t^i and not propagated. The other two normal modes are propagated using the equation of motion

$$m_Q \ddot{Q}_{iA} = -\frac{\partial E}{\partial Q_{iA}} = -\sum_{\alpha} C_{A\alpha} \frac{\partial E}{\partial q_{i\alpha}}, \tag{6.11}$$

where $C_{A\alpha}$ is the matrix from Equation 6.10. The value of m_Q is the same value used in the original TIP4P-FQ method [6.0x10^{-5}(ps/e)^{2}kcal/mol].[7] Once the normal modes have been propagated, new values of the charges can be found by inverting Equation 6.10, or

$$\begin{pmatrix} q_{iO} \\ q_{iH1} \\ q_{iH2} \end{pmatrix} = \begin{pmatrix} 1/3 & 0 & -1 \\ 1/3 & 1/2 & 1/2 \\ 1/3 & -1/2 & 1/2 \end{pmatrix} \begin{pmatrix} Q_{i1} \\ Q_{i2} \\ Q_{i3} \end{pmatrix}. \tag{6.12}$$

This method satisfies the charge constraint automatically by setting $Q_{i1} = Q_T^i$, so the undetermined multiplier never needs to be utilized.

Vita

Alexis J. Lee was born in Lake Charles, Louisiana, USA. She obtained her Bachelor of Science degree in Chemistry from the University of Louisiana, Lafayette, in 2006. Alexis started her Ph.D. program in the Department of Chemistry at the University of New Orleans in the fall of 2007, under the advisement of Professor Steve Rick in the field of computational chemistry.